A Deep Learning-based Workflow for the Automated Focal Mechanism Determination in Italy

F. Tavani[1*], P. Artale Harris[1], L. Scognamiglio[1*], M.-A.Meier[2]

1) Istituto Nazionale di Geofisica e Vulcanologia, INGV, Rome, Italy
2) Department of Earth and Planetary Sciences, Institut für Geophysik, ETH, Zurich, Switzerland

(*) Corresponding authors

Email Address: flavia.tavani@ingv.it, laura.scognamiglio@ingv.it

Abstract

The determination of earthquake focal mechanisms is crucial for understanding tectonic processes and assessing seismic hazard. While traditional methods based on manual polarity picking have proven effective, they are time-consuming and potentially subject to analyst's bias, particularly for small to moderate earthquakes. This study presents a machine learning-based approach for automating focal mechanism determination through P-wave polarity prediction. We develop and validate a methodology that combines a Convolutional Neural Network (CNN), based on the work by Ross et al. (2018) with the SKHASH algorithm (Skoumal et al. 2024), focusing on Italian earthquakes with magnitudes between 0 and 4.0, spanning the country's major active tectonic settings. The CNN, trained on a subset of the INSTANCE catalog by Michelini et al. (2021) containing over 450,000 Italian seismic waveforms, achieves 96% accuracy in polarity classification. To ensure the reliability of prediction, we implement stringent probability thresholds and validate our approach using a test dataset of 240,335 waveforms from 15,420 events. We then apply the methodology to 300 earthquakes with existing Time Domain Moment Tensor (TDMT) solutions finding a median Kagan angle (Kagan, 1991) between our FM and the TDMT solutions of 28.7°. This automated approach proves to be effective and may, in the future, offer a reliable means of determining focal mechanisms for lower magnitude events, where moment tensor inversions might not be feasible. This would contribute to a better understanding of regional seismotectonics and enhance seismic monitoring capabilities.

Key words. Earthquake parameterization, Machine Learning, Earthquake source

1. Introduction

Focal mechanisms provide fundamental information on earthquake source processes and the state of stress in the crust. For small magnitude earthquakes, large numbers of focal mechanisms allow detailed analyses of fault geometries, rupture kinematics, and fault zone behavior. When considered in aggregate, they reveal the spatial and temporal evolution of stress conditions, faulting styles and structural complexities within a region (Michael A., 1987; Nanjo, K.Z., 2020; Wang et al., 2020). Consequently, reliable focal mechanism solutions are essential for improving our understanding of regional seismotectonics and for supporting earthquake monitoring, especially in low seismicity areas (Imanishi et al., 2011; Imanishi et al. 2012; Matsumoto et al., 2015).

Accurate focal mechanism determination for moderate to large earthquakes are routinely and automatically determined by using full-wave moment tensor inversion techniques (Fukuyama et al., 1998; Ekstrom et al., 2012; Scognamiglio et al. 2006). However, it remains challenging for small-magnitude earthquakes due to difficulty of modelling high-frequency waveforms. In this regard, first-motion polarities approaches are used. Traditionally, these polarities are assigned manually through visual inspection of seismograms, a process that is time-consuming, susceptible to interpreter bias, and increasingly impractical as the volume of data from modern dense networks continues to grow.

To overcome these limitations, various automatic algorithms were developed prior to the advent of deep learning. Conventional approaches primarily relied on deterministic rules or statistical criteria applied to the waveform immediately following the P-wave arrival. Common techniques involved searching for the first extremum (local maximum/minimum) or zero-crossings to determine the sign of the motion (e.g., Nakamura, 2004; Chen and Holland, 2016). More advanced methods attempted to quantify the uncertainty of the polarity determination using

Bayesian approaches (Pugh et al., 2016) or were integrated into specific acquisition systems like the WIN system used in Japan (Urabe and Tsukada, 1991; Horiuchi et al., 2009)

While these approaches offer computational efficiency and interpretability, they often require site-specific parameter tuning, exhibit performance degradation in low signal-to-noise ratio environments, and generally fail to achieve the accuracy of expert manual processing. Their performance degrades significantly in low signal-to-noise ratio (SNR) environments or when dealing with emergent arrivals, where the first swing of the P-wave may be obscured by noise. These limitations have led to data-driven approaches based on Convolutional Neural Networks (CNNs), which can learn to extract relevant features directly from raw waveforms (Ross et al., 2018).

Machine Learning (ML) and specifically Deep Learning (DL) have emerged as powerful tools in seismology, capable of extracting high-level representations directly from raw waveform data without reliance on explicit, hand-coded rules. Convolutional Neural Networks (CNNs), originally designed for grid-structured data like images, have proven particularly effective for time-series analysis, enabling the automation of labor-intensive tasks such as earthquake detection and location (e.g., Perol et al., 2018; Mousavi et al., 2020) and phase picking (Zhu & Beroza, 2019).

In the specific context of source characterization, Ross et al. (2018) demonstrated the transformative potential of CNNs by introducing a model capable of determining P-wave first-motion polarities (FMP) with a precision comparable to human analysts. Their work paved the way for a rapid expansion of DL-based seismological methods, ranging from specialized architectures for polarity classification trained on large-scale datasets like INSTANCE (Chakraborty et al., 2022) to systems designed for real-time determination of focal mechanisms.

Following these methodologic advances, several studies have successfully applied DL algorithms to varied tectonic settings, from Japan (Hara et al., 2019; Uchide, 2020) to Southern California (Cheng et al., 2023) and Central Italy (Meier et al., 2025). These applications consistently demonstrate that data-driven approaches can produce more comprehensive and reliable focal mechanism catalogs than traditional automatic processing, even for small-magnitude events.

Building on these advances, this study evaluates a workflow that integrates deep learning-based P-wave polarity prediction with traditional focal mechanism estimation technique. We focus on the Italian Peninsula, an optimal region due its intense seismicity and dense seismic network (Margheriti et al. 2021).

We employ a CNN trained on INSTANCE, the high-quality Italian seismic dataset for ML (Michelini et al., 2021), and evaluate it on a completely independent dataset of 15,420 earthquakes that occurred in Italy between January 2021 and January 2025 (ML< 4.5), to ensure that no waveform used for testing was included during training or validation. The CNN provides both polarity classification and model probabilities, which we use to assess the confidence of each prediction. The predicted polarities are then input into the SKHASH algorithm (Skoumal et al. 2024) to compute focal mechanisms, which we evaluate against TDMT solutions catalog (Scognamiglio et al 2006, http://terremoti.ingv.it/tdmt).

While the work by Meier et al. (2025) has shown the potential of ML-derived focal mechanism catalogs for specific seismic sequences, here we assess the robustness and applicability of such a workflow across different tectonic environments in Italy. Our results provide a systematic evaluation of an automated, scalable, and data-driven approach to focal mechanism determination — one that has the potential to significantly enhance regional seismic monitoring capabilities.

2. Methodology

Convolutional neural networks (CNNs) are deep-learning architectures commonly used in supervised learning (Bishop 2006) that, unlike fully connected neural networks (Goodfellow et al., 2016), can process raw data directly through a series of convolutional and pooling layers, thus avoiding the need for manual feature extraction. The core of CNNs is the convolutional layer, which consists of learnable filters (kernels) designed to detect characteristic patterns across the input space. Filter coefficients, like other network parameters, are optimized during training to adapt to the target task.

This study starts from the CNN model developed by Ross et al. (2018) which was trained and tested using P-wave picks and first-motion polarities manually labeled by expert seismologists at the Southern California Seismic Network (SCSN). The training set was comprised of waveforms of earthquakes occurred in California from 2000 to 2017 (CalCat dataset, https://scedc.caltech.edu/data/deeplearning.html), while the test set was made of waveforms from the same time period, but which were not included in the training dataset. The model achieved pick times and polarity classification with a precision near 95%. Here, we retrain this CNN model on Italian seismic data, examine its performance and evaluate whether it improves the prediction capability on local test sets compared to the original California-based training dataset.

Our workflow integrates INGV web services (Bono et al., 2021) and the ObsPy library (Beyreuther et al., 2010) to retrieve earthquake hypocentral locations, waveform data, and analyst-picked P-wave arrival times. This section provides a detailed overview on the preparation of the training and test datasets.

2.1 Training Dataset Description

We created an Italian training dataset with waveform information along with P-wave arrival picks, derived from vertical component waveforms of velocimeters, with a balanced distribution of “up”, “down”, and “unknown” polarities. To achieve this goal, we used INSTANCE (Michelini et al., 2021), a dataset of seismic waveforms along with associated metadata, including P-wave arrival times, first motion polarities, and signal-to-noise ratio (SNR), suited for analysis based on machine learning techniques. While INSTANCE comprises approximately 1.2 million three-component waveform sets, recorded mainly by the Italian National Seismic Network from January 2005 to January 2020, our study extracts a subset of 824,131 individual vertical components (Z) from short and long period sensors (EH and HH channels). We accessed and processed these selections through Seisbench (Woollam et al., 2022), an open-source Python library that integrates INSTANCE among its supported datasets. The traces used in our training were manually classified by INGV analysts into three categories:

- 103,531 traces labeled as “up” (positive polarity);
- 57,668 traces labeled as "down" (negative polarity);
- 662,932 traces without assigned polarity, "unknown".

The unequal number of traces across the three categories results in an imbalanced dataset. To mitigate this, each trace with “up” and “down” polarity is included twice in the set, once in its original form and once by flipping it (i.e. multiplying it by -1). In this way we have 161,199 “up” traces (103,531 originals, and 57,668 obtained by flipping the “down” polarities) and the same number of “down” traces (57,668 originals, and 103,531 obtained by flipping the “up” polarities). Then, we selected 161,199 traces from the "unknown" category. As with any manually curated seismic catalog, an unassigned polarity does not necessarily imply that the first motion is intrinsically unclassifiable. In operational practice, polarity information may also be missing because sufficient observations have already been collected for the event or for other non-seismological reasons. To reduce this source of label uncertainty in the training set, only "unknown" traces with SNR < 3 were retained. The SNR was calculated as the ratio between the maximum absolute amplitudes measured in two symmetric 3-second windows, respectively preceding (noise) and following (signal) the P-wave arrival. This constraint was intended to preferentially include waveforms for which identifying the first-motion polarity was inherently challenging, while excluding as much as possible, traces whose missing polarity resulted from data redundancy, insufficient station coverage for focal mechanism solutions, or other operational considerations. The final training set is made of 483,597 traces equally divided among “up”, “down” and “unknown”, corresponding to 39,507 events that occurred between 2005 and 2020. Following Ross et al. (2018), we resampled the waveforms to 100 samples per second, detrended and applied a Butterworth filter with 4 poles between 1 and 20 Hz. The dataset adequately samples the variety of tectonic settings characterizing Italian seismicity (Latorre et al., 2023), as well as the most representative magnitude classes and typical source-to-station distances (Fig. 1, green).

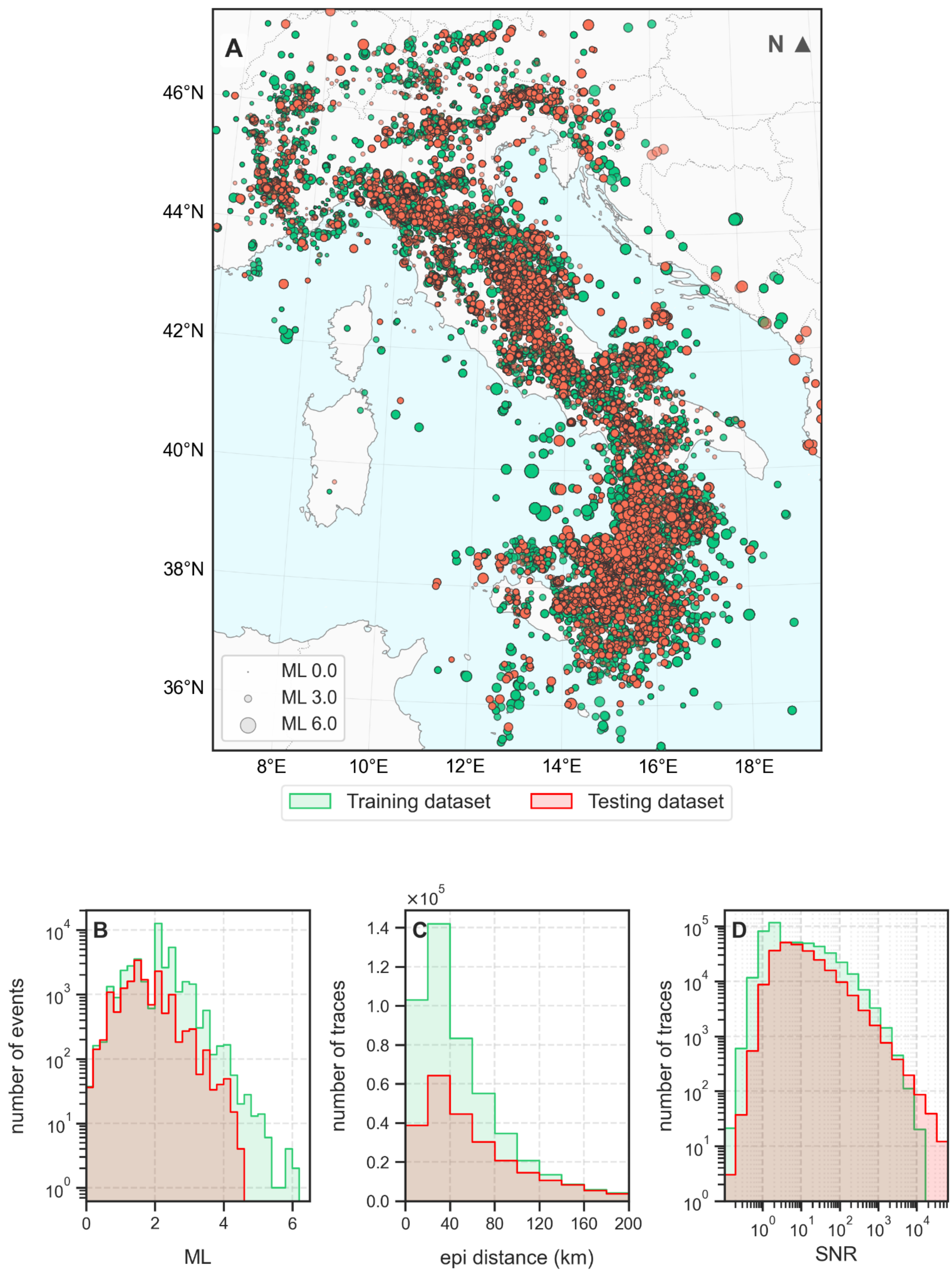
A
N
46°N
44°N
42°N
40°N
38°N
36°N
8°E
10°E
12°E
14°E
16°E
18°E
ML 0.0
ML 3.0
ML 6.0
Training dataset
Testing dataset
B
number of events
ML
C
$\times10^5$
number of traces
epi distance (km)
D
number of traces
SNR

Figure 1. Overview of the waveform datasets used for training (green) and testing (red). (A) Geographical distribution of seismic events; (B) Local magnitude (ML) range; (C) Epicentral distance distribution; (D) Signal-to-noise ratio (SNR) statistics.

We trained the CNN with this dataset obtaining what we called CNN_INSTANCE model. Following the methodology by Ross et al. (2018), we structured our training process as follows: the training data set was composed of 85% of the existing records, and the remaining 15% was left for validation. This division allowed us to maximize the amount of records used to train the model. We adopted the CNN model proposed by Ross et al. (2018), simplifying its architecture by reducing the last two fully connected layers to 20 neurons each, and slightly adjusting the training hyperparameters (batch size of 50 seismograms and a learning rate of 0.001). In addition to the polarity flipping, we implemented a further data augmentation technique where the 6-second feature window is randomly shifted 5 times by ±0.5 s relative to the P-wave arrival. By doing so, we force the network to learn invariant morphological characteristics of the P-wave onset rather than its absolute position in time, and we enlarge the training dataset up to 2,417,985 waveforms. This procedure significantly increases the effective training volume and prevents overfitting of the model to the noise, providing high classification precision even when the initial pick is not perfectly centered. Our training process took 50 epochs (Fig. S1 In Supplementary Material). We also verified that extending the training beyond 50 epochs with an early-stopping criterion did not produce a meaningful improvement in classification performance: the validation loss remains stable and the resulting confusion matrix remained nearly unchanged. Therefore, the model trained for 50 epochs was retained for the analyses presented below.

2.2 Test Dataset and Model Performance

To test our model, we prepared a completely independent dataset of Italian earthquakes, hereafter referred to as ItalyTest, with no overlap with the INSTANCE training dataset, both in terms of waveform content and acquisition period. We selected events from the Italian Seismic Bulletin (BSI, https://bsi.ingv.it/en/), whose locations, phase arrivals, and first-motion polarities are routinely reviewed by INGV seismologists, occurring between 1 January 2021 and 1 January 2025, with magnitudes ranging from ML 0 to 4.4 (Fig. 1, red). This temporal separation provides a realistic assessment of the model's ability to generalize to newly recorded seismic events under operational conditions. We retained only events for which at least one P-wave first-motion polarity had been manually assigned by an analyst. For each selected event, we extracted all vertical-component velocity traces recorded within a maximum epicentral distance of 200 km. This process yielded a dataset of 240,335 waveforms from 15,420 earthquakes. Overall, the dataset contains 47,812 manually assigned polarities (28,657 "up" and 19,155 "down"). The "unknown" class consists of two primary signal categories: (1) waveforms lacking a clear onset due to a low SNR, which makes the polarity emergence ambiguous; and (2) waveforms for which a polarity was not assigned due to standard analyst workflows. In the latter case, once a sufficient number of observations is reached to reliably constrain the focal mechanism or hypocenter, analysts may intentionally stop picking additional polarities to streamline the review process. Unlike the training dataset, no SNR-based selection was applied to the "unknown" class in the test dataset, which intentionally preserves the operational characteristics of BSI.

The CNN classification performance was evaluated using the confusion matrix (Fig. 2) together with the standard classification metrics of Precision, Recall, and Accuracy, defined as:

$$Precision = TP \,/\, (TP + FP) \quad (1)$$

$$Recall = TP \,/\, (TP + FN) \quad (2)$$

$$Accuracy = (TP + TN)/(TP + TN + FP + FN) \quad (3)$$

where TP, TN, FN and FP represent true positive, true negative, false negative and false positive respectively (Powers 2011, Kong et al., 2019).

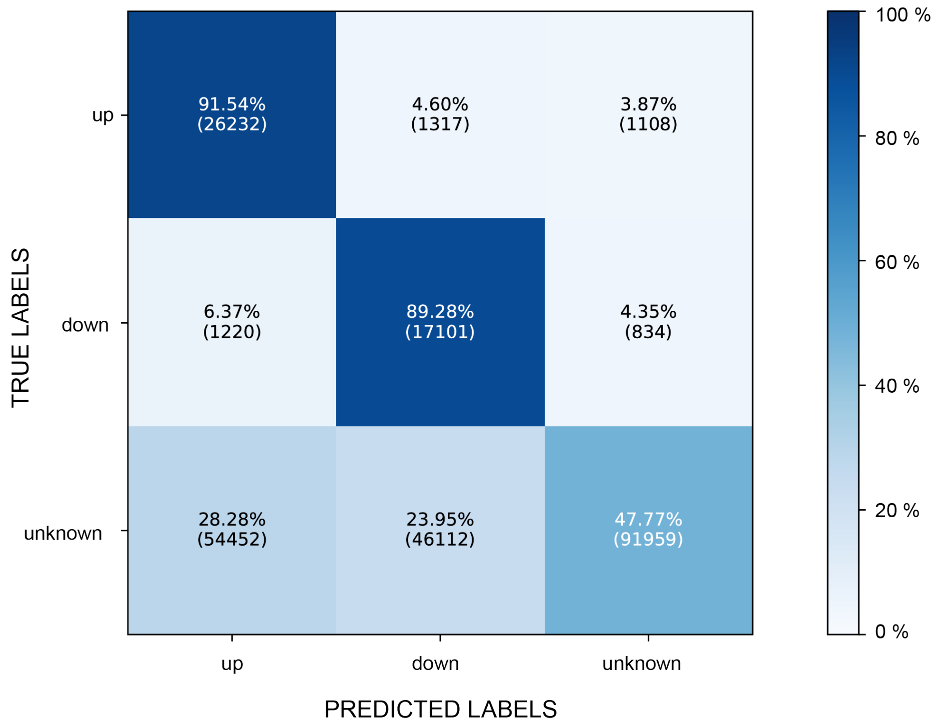

Figure 2. Confusion matrix of the CNN_INSTANCE model evaluated on the ItalyTest dataset. Values represent row-normalized percentages (totaling 100% per true class), with absolute trace counts provided in brackets.

Overall, the CNN model achieved a Precision of 95.6% and 93% for the "up" and "down" classes, respectively, with corresponding Recall values of 91.5% and 90%, and an overall Accuracy of 97%. In 52.23% of the cases originally labeled as "unknown" by the analysts, the CNN assigned either an "up" or "down" polarity. Since no reference polarity is available for these waveforms, their correctness cannot be assessed directly and they are therefore excluded from the performance metrics reported above. Nevertheless, these predictions highlight the model's ability to identify waveform characteristics that are consistent with first-motion polarities, even in cases where analysts were unable or did not assign a polarity.

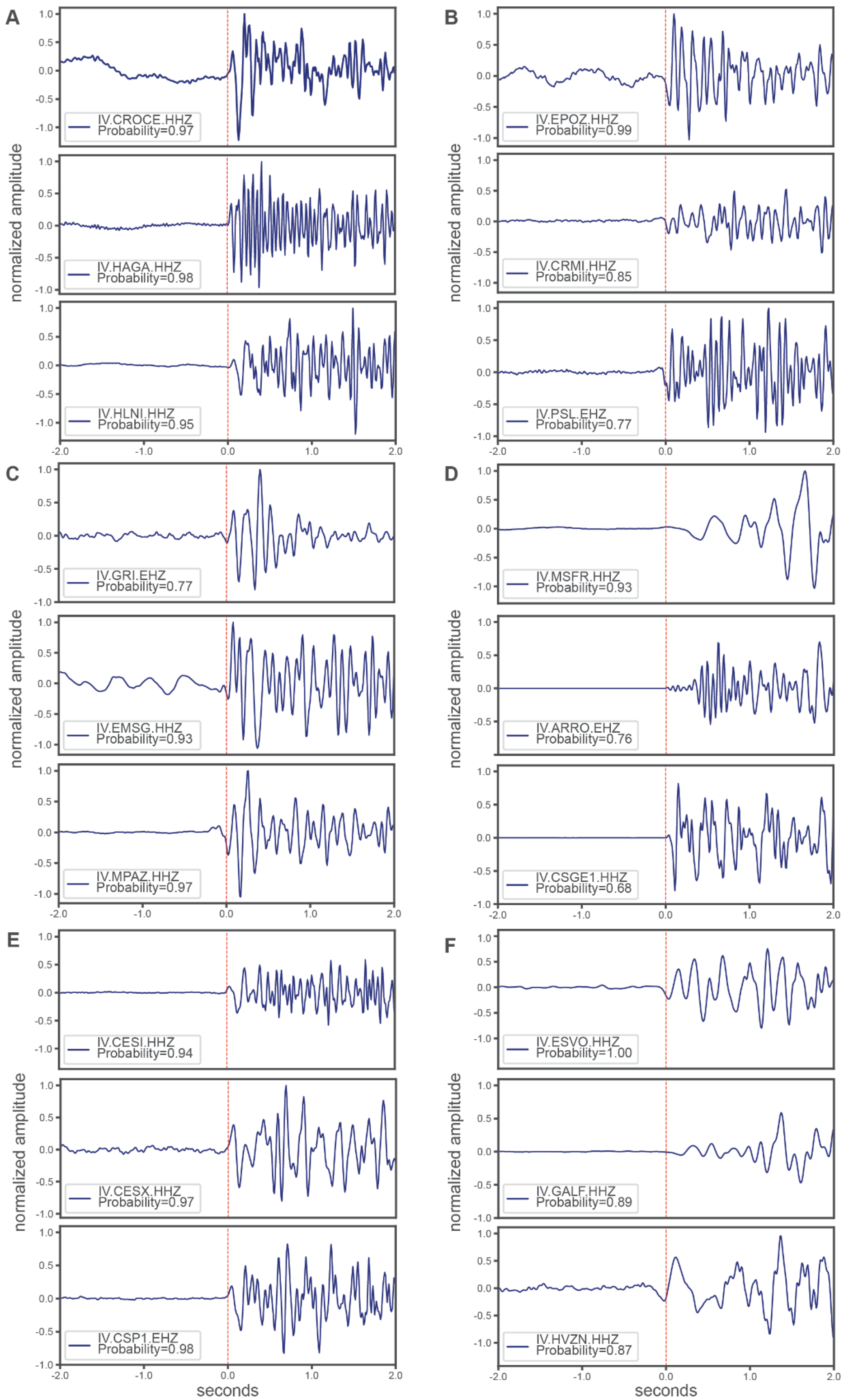

Figure 3: Examples of CNN-classified waveforms. Panels A and B show correctly classified "up" and "down" polarities, respectively. Panels C and D show polarity reversals relative to the manual labels, whereas Panels E and F show waveforms manually labeled as "unknown" but classified by the CNN as "up" and "down", respectively. Red lines are the analysts P-wave arrival picking.

Representative examples of all possible classification outcomes are shown in Fig. 3. Each panel contains three waveforms extracted from a 4 s time window centered on the P-wave arrival. For each waveform, the station code, the predicted polarity, and the corresponding confidence score (expressed as a probability) are reported. Panels A and B show traces where CNN's predictions match the analyst's “up” and “down” labels, respectively. Conversely, Panels C and D highlight some cases of opposite classifications. Such disagreements typically arise when the P onset is emergent or from imprecise P-wave pick positioning, which can cause the model to misinterpret the initial motion. Panels E and F show some cases of “recovered” polarities, for which the CNN classifies “up” or “down” when the assignment was “unknown”. Their reliability is further examined in the following section.

For completeness, the original CNN trained on the Southern California dataset (CNN_CalCat) was also evaluated on the ItalyTest dataset. The corresponding performance metrics and confusion matrix are presented in the Supplementary Material (Section S2.1 and Fig. S2). Compared with CNN_CalCat, the model retrained on the Italian INSTANCE dataset consistently achieves higher recall while maintaining comparable precision, correctly identifying an additional 1,924 first-motion polarities within the same test dataset. As shown in Fig. S2, this improvement mainly reflects the more conservative behavior of CNN_CalCat, which more frequently assigns an "unknown" label to waveforms with identifiable first-motion polarities. The improved performance suggests that region-specific training improves the model's ability to recognize the characteristics of Italian seismic waveforms. Based on these results, CNN_INSTANCE was adopted as the polarity classifier in the proposed workflow.

Finally, we evaluated the model performance by analyzing Precision and Recall as a function of the SNR, with values ranging from 0.6 to 1000 (Fig. 4). The Precision for both "up" and "down" classes consistently exceeds 90% and stabilizes at around 95% for data with high SNR values. This plateau should not be interpreted as a performance ceiling of the neural network, but rather as an indicator of the intrinsic noise in the labels of the test dataset (mislabeled polarities) or inherent signal complexities that persist regardless of signal clarity. The Recall, instead, generally increases with SNR, for up and down classes, while it decreases for the “unknown” class. Specifically, the Recall for polarity classes rises from approximately 40% at SNR = 1 to a stable 90% for SNR≥10, while for “unknown” traces it rapidly drops toward zero as the SNR reaches 100. This lower Recall compared to Precision suggests that when the classification is uncertain due to a low SNR, the network behaves conservatively: the model's strategy is to ensure the reliability of its positive predictions ("up" or "down") by sacrificing the ability to find all possible instances of those polarities, especially in noisy conditions.

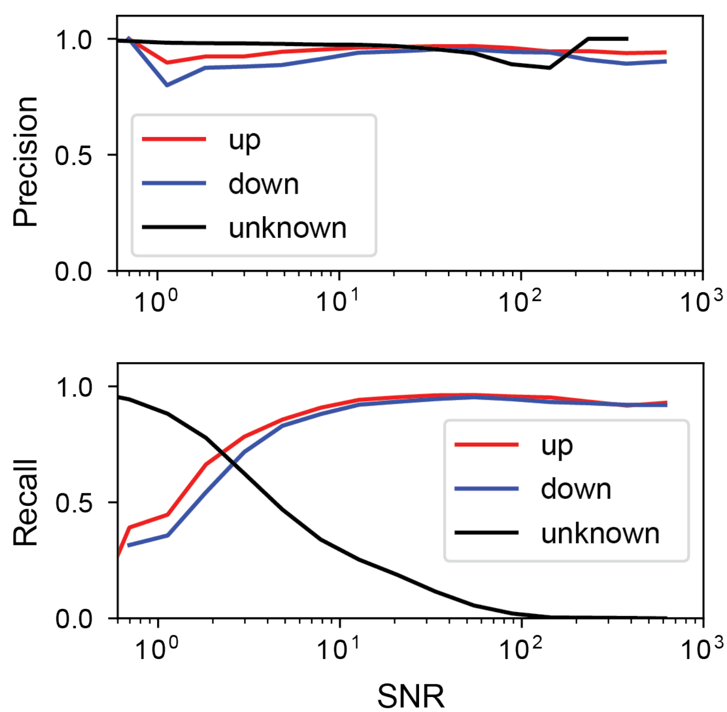

Figure 4. Trend of Precision and Recall metrics as a function of SNR.

2.3 Selection of the Operational Probability Threshold

In focal mechanism inversion, polarity reversal errors are considerably more detrimental than missing observations, as even a small number of incorrect first-motion polarities may lead to erroneous source solutions. Consequently, the objective is not simply to maximize the classification performance of the CNN, but to maximize the number of reliable polarity measurements available for focal mechanism computation. To achieve this, we use the probability associated with each CNN prediction (i.e., the Softmax output) as a measure of classification confidence, rather than relying on conventional signal-to-noise ratio (SNR) thresholds. This choice follows the work of Hara et al. (2019), who showed that the prediction probability is strongly correlated with the actual classification accuracy. For every waveform, the CNN outputs a normalized probability distribution over the three classes ("up", "down", and "unknown"), whose values sum to one.

The reliability of these probabilities is illustrated in Fig. 5, which shows their distributions for all combinations of predicted and manually assigned labels. Correctly classified "up" and "down" polarities (panels A and E) are characterized by probability distributions strongly concentrated near one, indicating that the CNN assigns high confidence to correct predictions. In contrast, misclassified polarities (panels B–F) exhibit broader distributions shifted toward lower probability values, suggesting that erroneous classifications are generally associated with lower confidence. Interestingly, waveforms originally left unlabeled by the analysts but classified as "up" or "down" by the CNN (panels G and H) display distributions that are noticeably more skewed toward high probabilities than the corresponding misclassified cases (panels B and D). This observation suggests that many of these waveforms contain recognizable first-motion information rather than representing intrinsically ambiguous arrivals. Overall, these results demonstrate that the Softmax probability provides a meaningful estimate of the reliability of the predicted polarity.

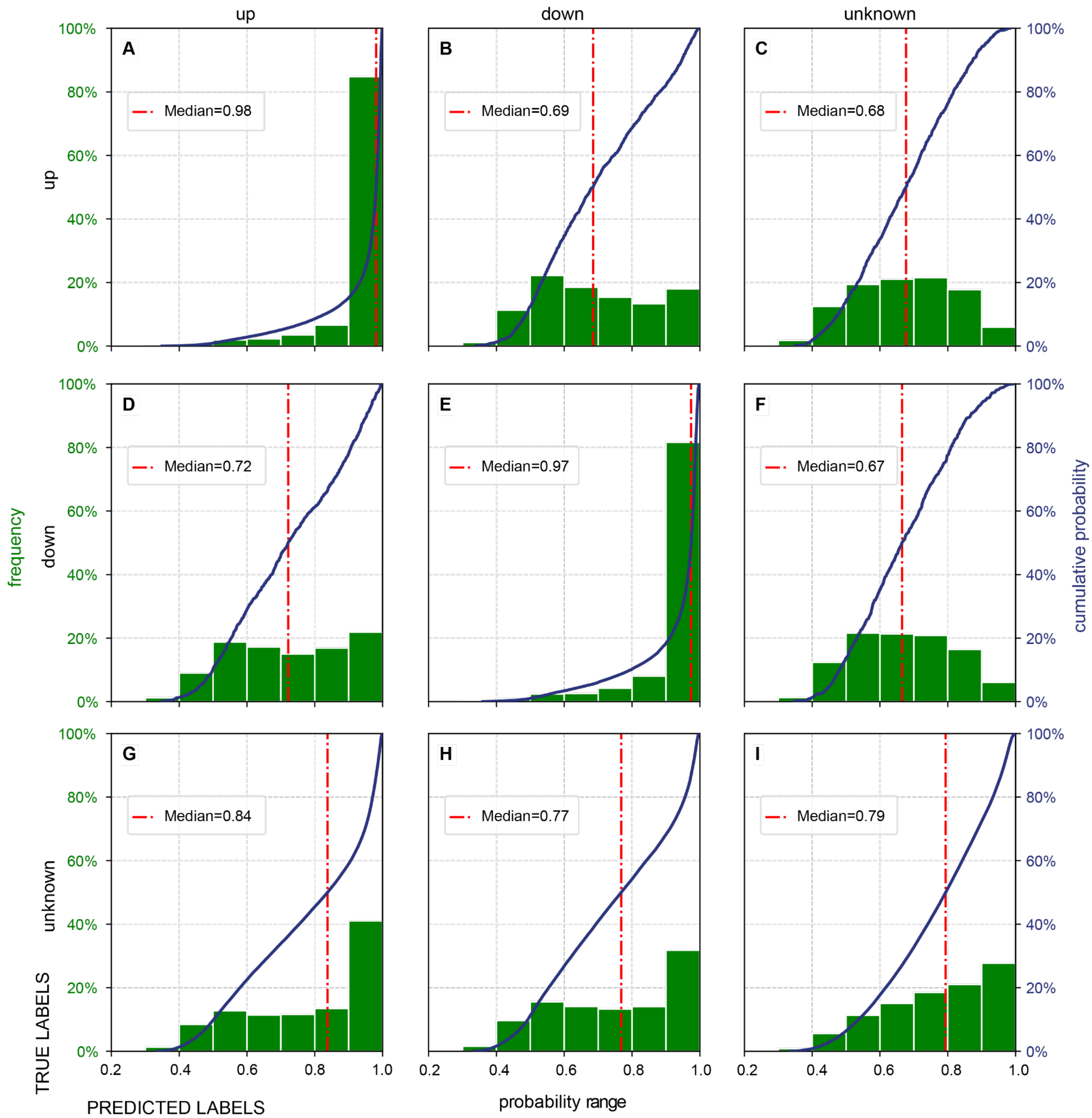

Figure 5. Probability distributions associated with the CNN predictions for each combination of manually assigned (rows) and predicted (columns) polarity labels. Green histograms represent

the probability distributions, blue curves the cumulative distributions, and the red dashed lines the median probability values.

The selection of the probability threshold therefore represents a trade-off between two competing objectives: maximizing the reliability of the predicted polarities while preserving a sufficient number of observations for focal mechanism inversion. Increasing the threshold progressively improves precision but simultaneously reduces the number of retained polarity picks (Fig. 6). In conventional machine-learning applications, this trade-off is commonly addressed by selecting the threshold that maximizes the F1-score. However, this criterion is not appropriate for our application, maximizing the F1-score would suggest a threshold greater than 0.94, the corresponding increase in precision is marginal, whereas the number of retained polarity observations decreases dramatically. Since reliable focal mechanism solutions require adequate azimuthal coverage, discarding such a large fraction of the available observations would substantially reduce the applicability of the workflow.

Instead, we selected the operational threshold by requiring a precision close to 98% while retaining at least 80% of the predicted polarities. As shown in Fig. 6, a probability threshold of 0.85 provides the best balance between these competing requirements. This value corresponds to the onset of the rapid decrease in retained observations, while further increases in the threshold yield only marginal improvements in precision.

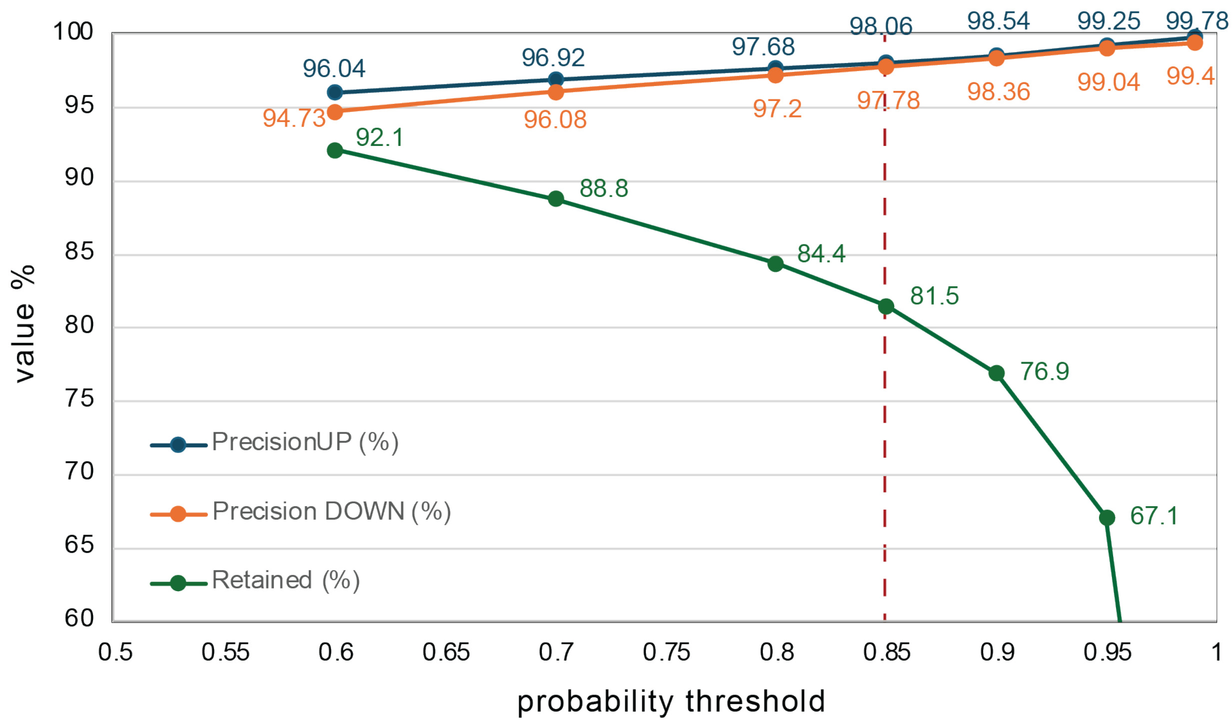

Figure 6. Precision for the "up" and "down" polarity classes and percentage of retained predictions as a function of the probability threshold. The dashed red line indicates the selected probability threshold (0.85).

Applying this threshold substantially improves the quality of the polarity dataset used for focal mechanism inversion (Fig. 7). Misclassified "down" polarities predicted as "up" decrease from 1,220 to 380, while misclassified "up" polarities predicted as "down" decrease from 1,317 to 320. As a result, Precision increases to 98.4% and 97.9% for the "up" and "down" classes, respectively, while Recall reaches 97.9% and 96.8%.

.

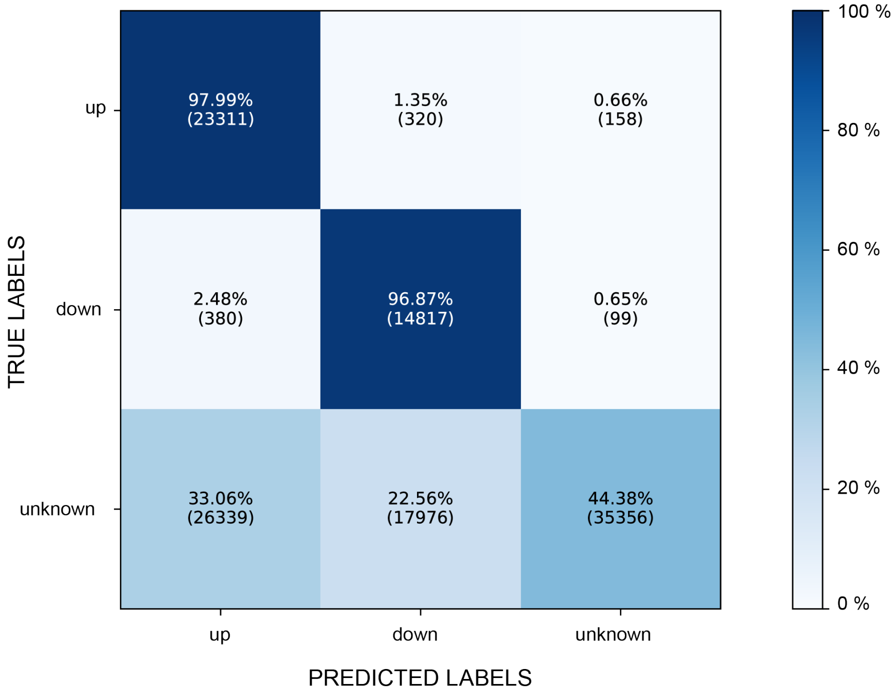

Figure 7. Confusion matrix for the CNN_INSTANCE model restricted to classifications with a probability score exceeding 0.85. Each cell displays the row-normalized percentage and the absolute number of traces (in brackets).

Although the threshold excludes 257 manually assigned polarities, it also recovers 44,315 high-confidence "up" and "down" polarities from waveforms that had originally been left unlabeled by the analysts (Fig. 8). This substantial increase in reliable polarity observations represents one of the principal advantages of the proposed workflow, providing a significantly richer dataset for subsequent focal mechanism inversion while maintaining a very high level of classification reliability.

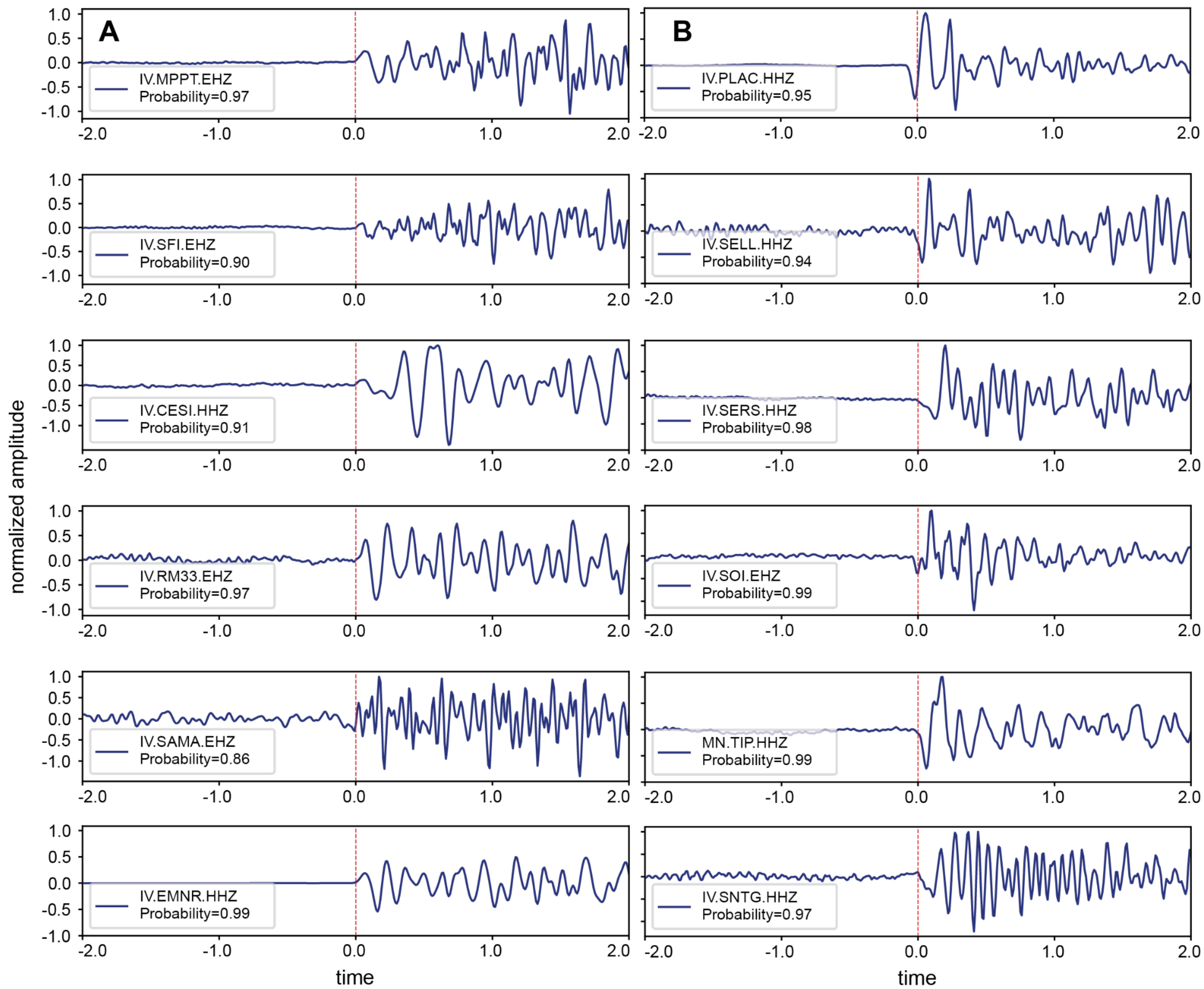

Figure 8: Randomly selected waveforms with "unknown" manual labels classified by the CNN as (A) "up" and (B) "down" polarity.

3 Workflow Implementation

This section outlines the step-by-step procedure implemented in our study, as illustrated in the comprehensive workflow diagram of Fig. 9.

The first stage involves retrieving earthquake hypocentral data and waveforms using a combination of INGV web services (https://terremoti.ingv.it/webservices_and_software) and the

ObsPy library (Beyreuther et al., 2010). We use the *fdsnws-event* API to extract reviewed origin information, including latitude, longitude, depth, and the P-wave arrival times having an uncertainty of less than one second. For all stations having distance from the epicenter ≤ 200 km, we download vertical velocity waveforms, within a 20-second time window before and after the event origin time, using the ObsPy *get_waveforms* service. The waveforms are resampled to 100 samples per second, detrended, and processed with a Butterworth band-pass filter between 1 and 20 Hz with 4 poles. We then extract a 6-second window centered on the P-wave arrival time for each station. The resulting waveforms and metadata are stored in a standardized HDF5 format.

In the second stage, the pre-processed HDF5 files are processed by the CNN_INSTANCE model. The network analyzes the waveforms to classify the first-motion polarities as “up” “down” or “unknown”. Crucially, the model outputs a list of positive, negative or unknown polarities, with the corresponding a posterior probability distribution, providing a quantitative measure of the network's confidence in each assignment.

The third stage involves a rigorous selection process based on the Step 2 output probabilities. Polarity assignments are filtered using the optimized thresholds established in Section 2.3. We discard all “unknown” labels and any “up”/”down” predictions that fall below the assigned probability threshold. This ensures that only high-confidence picks are utilized for the subsequent source inversion.

Finally, the selected polarities are used to compute the focal mechanism via the SKHASH algorithm (Skoumal et al. 2024), a Python implementation based on the well-established HASH code (Hardebeck & Shearer, 2002). The HASH algorithm determines a suite of potential solutions based on the provided P-wave polarities and S/P ratio measurements. Given an event's hypocenter, station geometry, a seismic velocity model, and observed P-wave first-motion polarities, HASH computes takeoff angles for each station. Then it performs a grid search across a discrete range of strike, dip, and rake values to identify focal mechanism solutions that optimize polarity fit.

SKHASH introduces several advanced features over its predecessor, including more flexible input formats and enhanced computational efficiency, making it better suited for modern seismological workflows. A key methodological improvement is that while HASH only accounts for variations in the hypocentral depth, SKHASH incorporates 3D hypocentral variations, allowing for more realistic changes in source-receiver azimuths. Furthermore, SKHASH assigns a specific weight to each polarity measurement based on its contributions to the final solution. By default, the algorithm assigns a weight of 1.0 to impulsive polarity and 0.5 to the emergent ones. Since we already filtered the most reliable polarities and our CNN does not currently distinguish between emergent or impulsive arrivals, we characterized all predicted first arrivals as impulsive, assigning to them a uniform weight of 1.0. Consequently, the weighting of phases becomes irrelevant. For this study, the inversion was performed using P-wave polarities and the CIA1D velocity model (Herrmann et al., 2011).

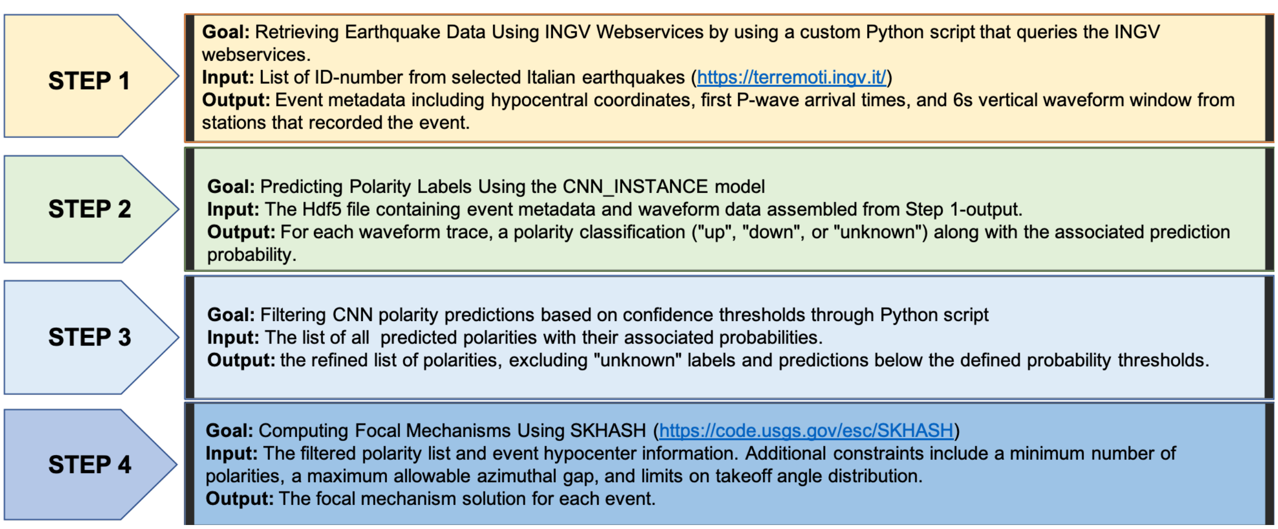

Figure 9. Flowchart illustrating the main stages of the methodological workflow. For each processing step, the respective input and output data are specified.

4 Application - Comparisons between workflow solutions and TDMT solutions

To evaluate the reliability of our automated workflow, we conducted a comparative analysis between our predicted focal mechanisms and the double-couple components provided by the Time Domain Moment Tensor (TDMT) catalog (https://terremoti.ingv.it/tdmt?timezone=UTC, Scognamiglio et al., 2009). The TDMT solutions serve as our primary benchmark, as they are initially generated automatically (within 6 to 9 minutes of origin time), and subsequently refined through manual review by INGV analysts. For this validation, we specifically targeted events for which a high-quality TDMT solution already exists, allowing us to assess how closely our CNN-based approach replicates expert-validated results. From the comprehensive INGV database, we selected a subset of 300 events based on the following criteria:

- Occurrence between January 1, 2014, and December 31, 2024;
- Moment magnitude Mw $\leq$ 4.5;
- Inland location within the Italian territory to ensure optimal station coverage and avoid offshore path complexities;
- High quality TDMT indices (Aa, Ab, or Ba);
- Hypocentral depth $\leq$ 20 km.

The evaluation process follows the workflow described in Section 3: for each event, the CNN predicts first-motion polarities filtering for those that meet our established probability thresholds. SKHASH then performs a grid search across a depth range of ±2 km (in 1 km increments) centered on the TDMT depth. To ensure well-constrained solutions, we enforced several quality constraints within SKHASH: a minimum of 10 valid polarities, a maximum takeoff angle of 90°, and maximum azimuthal gap 150°. Among the initial events analyzed, 47 were excluded because they didn't meet these stringent requirements: 28 lacked the minimum number of CNN-predicted polarities, while 19 exceeded the azimuthal gap limit.

To select the preferred focal mechanism depth, and to quantify the similarity between our derived solutions and the reference catalog, we utilized the Kagan angle (Kagan, 1991). The depth that minimizes the Kagan angle is selected as the best-fit solution. Following established benchmarks in recent deep learning studies (e.g., Cheng et al., 2023; Meier et al., 2025), we consider mechanisms with a Kagan angle ≤ 25-30° to be in strong agreement, while values up to 40-45° are considered acceptable within the typical uncertainties of routine focal mechanism determination (Zhao et al., 2023). The Kagan angles distribution is notably skewed toward lower values (Fig. 10), with most events following between 10° and 30°, and a median value of 28.7°, indicating excellent agreement with the TDMT catalog.

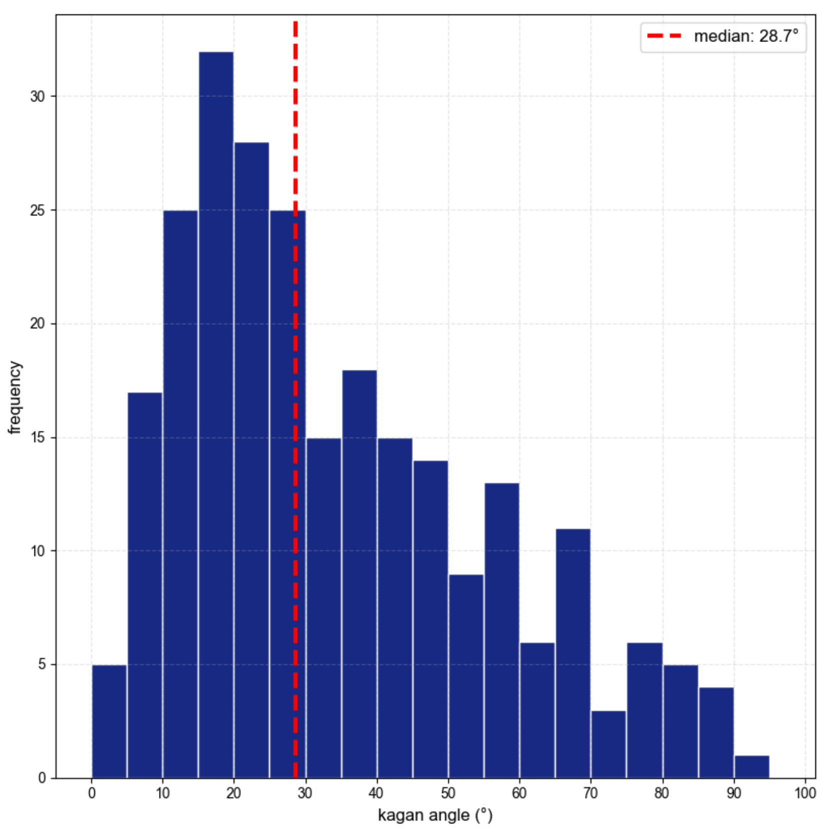

Figure 10. Distribution of Kagan angles between the predicted and TDMT focal mechanism solutions for the 253 test event, and its median value.

Overall, 165 of the 253 events yielded a Kagan angle below 40° , a threshold that is indicative of a good agreement, while 15 fall in the 40-45° range (Fig. 11). The high degree of visual and statistical similarity confirms that our methodology is capable of producing reliable and physically consistent focal mechanism solutions automatically. Events with Kagan angles larger than 40° are reported and discussed in the Supplementary Material (Section S3 and Fig. S4).

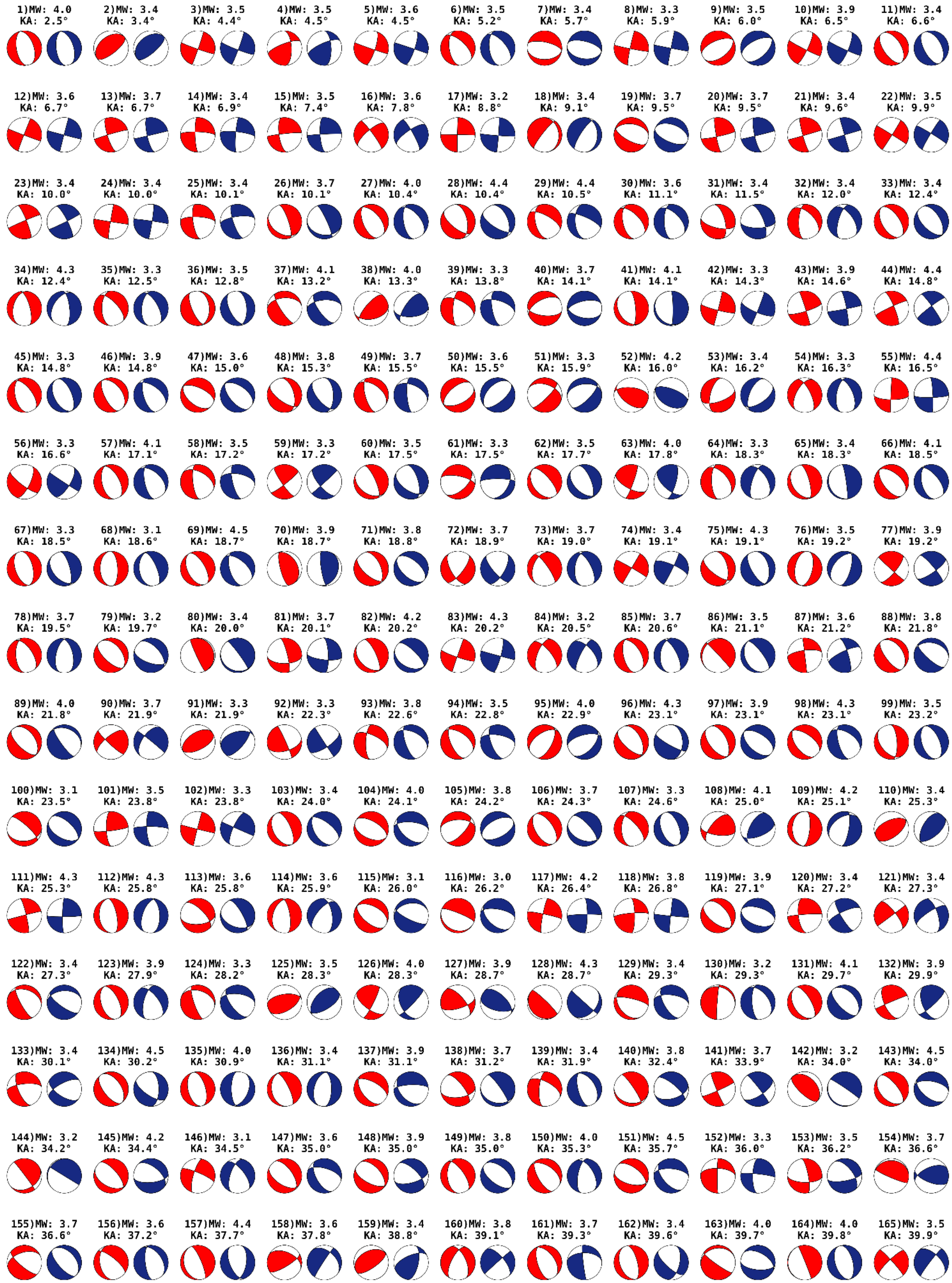
1)MW: 4.0 KA: 2.5°
2)MW: 3.4 KA: 3.4°
3)MW: 3.5 KA: 4.4°
4)MW: 3.5 KA: 4.5°
5)MW: 3.6 KA: 4.5°
6)MW: 3.5 KA: 5.2°
7)MW: 3.4 KA: 5.7°
8)MW: 3.3 KA: 5.9°
9)MW: 3.5 KA: 6.0°
10)MW: 3.9 KA: 6.5°
11)MW: 3.4 KA: 6.6°
12)MW: 3.6 KA: 6.7°
13)MW: 3.7 KA: 6.7°
14)MW: 3.4 KA: 6.9°
15)MW: 3.5 KA: 7.4°
16)MW: 3.6 KA: 7.8°
17)MW: 3.2 KA: 8.8°
18)MW: 3.4 KA: 9.1°
19)MW: 3.7 KA: 9.5°
20)MW: 3.7 KA: 9.5°
21)MW: 3.4 KA: 9.6°
22)MW: 3.5 KA: 9.9°
23)MW: 3.4 KA: 10.0°
24)MW: 3.4 KA: 10.0°
25)MW: 3.4 KA: 10.1°
26)MW: 3.7 KA: 10.1°
27)MW: 4.0 KA: 10.4°
28)MW: 4.4 KA: 10.4°
29)MW: 4.4 KA: 10.5°
30)MW: 3.6 KA: 11.1°
31)MW: 3.4 KA: 11.5°
32)MW: 3.4 KA: 12.0°
33)MW: 3.4 KA: 12.4°
34)MW: 4.3 KA: 12.4°
35)MW: 3.3 KA: 12.5°
36)MW: 3.5 KA: 12.8°
37)MW: 4.1 KA: 13.2°
38)MW: 4.0 KA: 13.3°
39)MW: 3.3 KA: 13.8°
40)MW: 3.7 KA: 14.1°
41)MW: 4.1 KA: 14.1°
42)MW: 3.3 KA: 14.3°
43)MW: 3.9 KA: 14.6°
44)MW: 4.4 KA: 14.8°
45)MW: 3.3 KA: 14.8°
46)MW: 3.9 KA: 14.8°
47)MW: 3.6 KA: 15.0°
48)MW: 3.8 KA: 15.3°
49)MW: 3.7 KA: 15.5°
50)MW: 3.6 KA: 15.5°
51)MW: 3.3 KA: 15.9°
52)MW: 4.2 KA: 16.0°
53)MW: 3.4 KA: 16.2°
54)MW: 3.3 KA: 16.3°
55)MW: 4.4 KA: 16.5°
56)MW: 3.3 KA: 16.6°
57)MW: 4.1 KA: 17.1°
58)MW: 3.5 KA: 17.2°
59)MW: 3.3 KA: 17.2°
60)MW: 3.5 KA: 17.5°
61)MW: 3.3 KA: 17.5°
62)MW: 3.5 KA: 17.7°
63)MW: 4.0 KA: 17.8°
64)MW: 3.3 KA: 18.3°
65)MW: 3.4 KA: 18.3°
66)MW: 4.1 KA: 18.5°
67)MW: 3.3 KA: 18.5°
68)MW: 3.1 KA: 18.6°
69)MW: 4.5 KA: 18.7°
70)MW: 3.9 KA: 18.7°
71)MW: 3.8 KA: 18.8°
72)MW: 3.7 KA: 18.9°
73)MW: 3.7 KA: 19.0°
74)MW: 3.4 KA: 19.1°
75)MW: 4.3 KA: 19.1°
76)MW: 3.5 KA: 19.2°
77)MW: 3.9 KA: 19.2°
78)MW: 3.7 KA: 19.5°
79)MW: 3.2 KA: 19.7°
80)MW: 3.4 KA: 20.0°
81)MW: 3.7 KA: 20.1°
82)MW: 4.2 KA: 20.2°
83)MW: 4.3 KA: 20.2°
84)MW: 3.2 KA: 20.5°
85)MW: 3.7 KA: 20.6°
86)MW: 3.5 KA: 21.1°
87)MW: 3.6 KA: 21.2°
88)MW: 3.8 KA: 21.8°
89)MW: 4.0 KA: 21.8°
90)MW: 3.7 KA: 21.9°
91)MW: 3.3 KA: 21.9°
92)MW: 3.3 KA: 22.3°
93)MW: 3.8 KA: 22.6°
94)MW: 3.5 KA: 22.8°
95)MW: 4.0 KA: 22.9°
96)MW: 4.3 KA: 23.1°
97)MW: 3.9 KA: 23.1°
98)MW: 4.3 KA: 23.1°
99)MW: 3.5 KA: 23.2°
100)MW: 3.1 KA: 23.5°
101)MW: 3.5 KA: 23.8°
102)MW: 3.3 KA: 23.8°
103)MW: 3.4 KA: 24.0°
104)MW: 4.0 KA: 24.1°
105)MW: 3.8 KA: 24.2°
106)MW: 3.7 KA: 24.3°
107)MW: 3.3 KA: 24.6°
108)MW: 4.1 KA: 25.0°
109)MW: 4.2 KA: 25.1°
110)MW: 3.4 KA: 25.3°
111)MW: 4.3 KA: 25.3°
112)MW: 4.3 KA: 25.8°
113)MW: 3.6 KA: 25.8°
114)MW: 3.6 KA: 25.9°
115)MW: 3.1 KA: 26.0°
116)MW: 3.0 KA: 26.2°
117)MW: 4.2 KA: 26.4°
118)MW: 3.8 KA: 26.8°
119)MW: 3.9 KA: 27.1°
120)MW: 3.4 KA: 27.2°
121)MW: 3.4 KA: 27.3°
122)MW: 3.4 KA: 27.3°
123)MW: 3.9 KA: 27.9°
124)MW: 3.3 KA: 28.2°
125)MW: 3.5 KA: 28.3°
126)MW: 4.0 KA: 28.3°
127)MW: 3.9 KA: 28.7°
128)MW: 4.3 KA: 28.7°
129)MW: 3.4 KA: 29.3°
130)MW: 3.2 KA: 29.3°
131)MW: 4.1 KA: 29.7°
132)MW: 3.9 KA: 29.9°
133)MW: 3.4 KA: 30.1°
134)MW: 4.5 KA: 30.2°
135)MW: 4.0 KA: 30.9°
136)MW: 3.4 KA: 31.1°
137)MW: 3.9 KA: 31.1°
138)MW: 3.7 KA: 31.2°
139)MW: 3.4 KA: 31.9°
140)MW: 3.8 KA: 32.4°
141)MW: 3.7 KA: 33.9°
142)MW: 3.2 KA: 34.0°
143)MW: 4.5 KA: 34.0°
144)MW: 3.2 KA: 34.2°
145)MW: 4.2 KA: 34.4°
146)MW: 3.1 KA: 34.5°
147)MW: 3.6 KA: 35.0°
148)MW: 3.9 KA: 35.0°
149)MW: 3.8 KA: 35.0°
150)MW: 4.0 KA: 35.3°
151)MW: 4.5 KA: 35.7°
152)MW: 3.3 KA: 36.0°
153)MW: 3.5 KA: 36.2°
154)MW: 3.7 KA: 36.6°
155)MW: 3.7 KA: 36.6°
156)MW: 3.6 KA: 37.2°
157)MW: 4.4 KA: 37.7°
158)MW: 3.6 KA: 37.8°
159)MW: 3.4 KA: 38.8°
160)MW: 3.8 KA: 39.1°
161)MW: 3.7 KA: 39.3°
162)MW: 3.4 KA: 39.6°
163)MW: 4.0 KA: 39.7°
164)MW: 4.0 KA: 39.8°
165)MW: 3.5 KA: 39.9°

Figure 11. Focal mechanisms for 165 events with Kagan Angle < 40°. Blue: proposed methodology; Red: TDMT catalog. Labels above each pair are moment magnitude (M_W) and the Kagan angle (KA) between the two mechanisms. The correspondence between each mechanism number and its associated event identifier in the INGV web-site (https://terremoti.ingv.it/) is provided in Table S1 (Supplementary Material).

To further evaluate the quality of the CNN-derived focal mechanism catalog, we analyzed the percentage of misfitting polarities for each of the 253 event's best-fitting solution, as provided by SKHASH code.The misfit polarity indicate the internal consistency between the observed polarities and the theoretical radiation pattern, a misfit of 0% represents a perfect agreement. To establish a baseline, we also performed the SKHASH inversion on the initial 300 events using polarities manually assigned by analysts and applying the same quality constraints (minimum of 10 valid polarities, maximum takeoff angle and maximum azimuthal gap of 90° and 150° respectively). Under these constraints, the manual dataset yielded 209 focal mechanisms, 44 fewer than the CNN-derived. The distribution of the CNN-derived misfit follows a trend remarkably similar to that of the manual picks, which we consider the ground truth (Fig. 12). This similarity confirms that the CNN-predicted polarities are as reliable as those provided by expert analysts. Furthermore, the majority of the extra mechanisms recovered by the CNN shows a misfit below 20%, with a prominent peak around 10%. These results demonstrate that our automated workflow not only significantly expands the number of available focal mechanisms but also ensures they meet high standards of physical consistency and reliability.

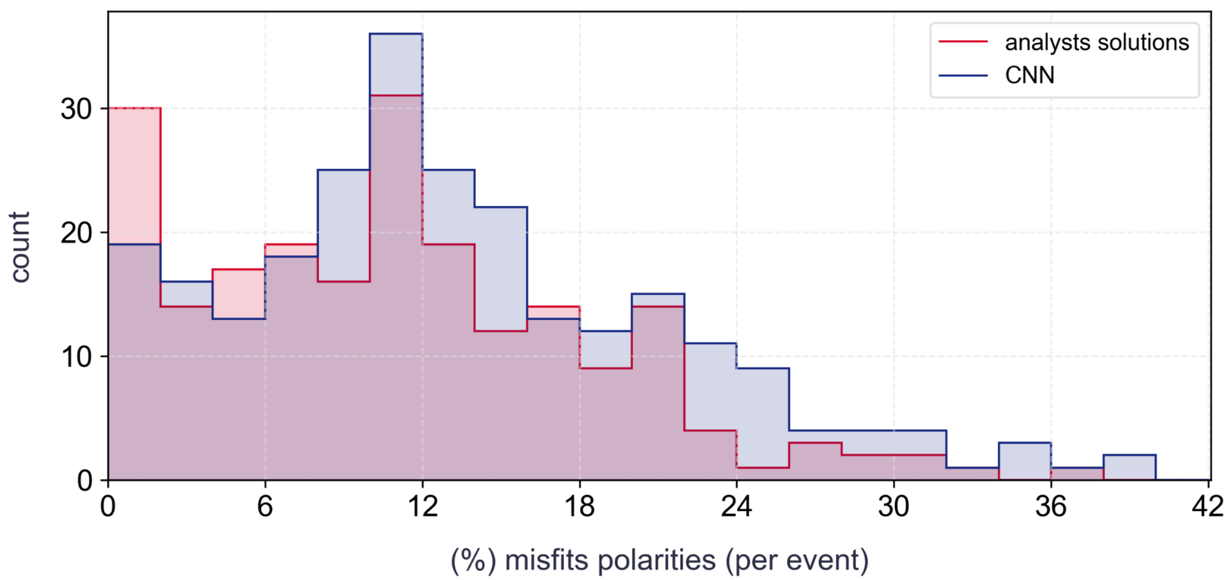

Figure 12. Comparison of the polarity misfit parameters for focal mechanisms obtained using the automated (CNN_INSTANCE) and the manual analyst (INGV catalog) polarity datasets.

5. Discussion

The primary outcome of this study is the indication that a deep learning–based polarity classifier can be successfully integrated into an operational workflow for automated focal mechanism determination. Rather than developing a new neural network architecture, our objective was to evaluate whether the CNN proposed by Ross et al. (2018), if retrained on region-specific seismic data, could provide reliable polarity information for routine focal mechanism computation in Italy. The results demonstrate that this objective is achieved by combining three key elements: (i) regional training of the CNN, (ii) probability-based selection of reliable polarity measurements, and (iii) integration with the SKHASH inversion algorithm.

To place these results in context, we compare the performance of our workflow with two reference studies. The first is the original work of Ross et al. (2018), in which CNN was trained on Southern California data. The second is the study by Chakraborty et al. (2022), who proposed an architecture trained both on Southern California data and on the Italian INSTANCE dataset. Together, these studies provide a suitable benchmark for evaluating both the classification performance of the retrained CNN and the effectiveness of its integration into an operational workflow. Based on this reference, our network is expected to reach a Precision higher than 95%, while Recall may range between 80% and 98%, depending on how conservative the model is. Our model attains precision values of 98.4% (“up”) and 97.9% (“down”), and recall values of 97.9% and 96.8%, respectively, placing its performance well within the current state of the art. As discussed below, these values are obtained after applying a confidence-based selection of the CNN predictions, a key component of the proposed workflow.

Although the CNN architecture was originally developed for Southern California, the comparison between the CNN retrained on the Italian INSTANCE dataset (CNN_INSTANCE) and the original model (CNN_CalCat) clearly highlights the importance of region-specific training. Since both models are based on the same architecture, the retrained network consistently achieves higher recall while maintaining comparable precision, indicating that its improved performance arises from a better adaptation to the characteristics of Italian seismic waveforms rather than from changes in the network design. This behavior is particularly evident for waveforms that remained unlabeled in the Italian Seismic Bulletin, where CNN_INSTANCE recovered more than 44,000 additional high-confidence "up" and "down" polarities. In contrast, CNN_CalCat adopts a more conservative strategy, more frequently assigning the "unknown" label to waveforms containing identifiable first-motion information. These results suggest that regional training not only improves classification performance but also extends the amount of information available for focal mechanism inversion. However, increasing the number of polarity measurements is beneficial only if their reliability can be guaranteed.

To achieve this, the proposed workflow exploits the probability associated with each CNN prediction as an estimate of its confidence. Only predictions exceeding a predefined confidence threshold are retained for focal mechanism inversion. The definition of this threshold, however, cannot rely exclusively on conventional machine-learning criteria as by maximizing a statistical metric such as the F1-score. For focal mechanism inversion, this criterion is not necessarily appropriate because the objective is not simply to maximize classification accuracy, but to maximize the number of reliable polarity observations while preserving the station coverage required to constrain the focal sphere.

For this reason, we selected the probability threshold according to requirements of focal mechanism determination rather than purely statistical criteria. The adopted threshold ($p \geq 0.85$) provides an effective balance between polarity reliability and data availability, preserving more than 80% of the observations while achieving a precision close to 98%. Although higher thresholds would produce marginal gains in precision, they would, in contrast, substantially reduce the number of usable polarity measurements, ultimately degrading the stability of the focal mechanism inversion. This result highlights that the optimal probability threshold should not be selected solely on the basis of conventional machine-learning metrics. Instead, it should reflect the requirements of the focal mechanism inversion, where preserving a sufficiently large and geometrically well-distributed set of reliable polarity observations is more important than maximizing the classification performance of the CNN itself.

The effectiveness of the proposed workflow is demonstrated through comparison with the expert-reviewed TDMT catalogue, which provides an independent benchmark for assessing the reliability of the computed focal mechanisms. The strong agreement observed for a significant portion of the catalogue indicates that the combination of region-specific training, confidence-based polarity selection, and SKHASH inversion produces physically consistent focal mechanism solutions across a wide range of tectonic settings in Italy. Events associated with the largest Kagan angles are not primarily the result of incorrect polarity predictions. Instead, as discussed in the Supplementary Material, these discrepancies are largely explained by factors intrinsic to the kinematic parameters' estimation problem, including limited station coverage, unfavorable takeoff-angle distributions, and an insufficient or strongly unbalanced set of polarity observations.

Such conditions reduce the stability of the focal mechanism solution regardless of the accuracy of the polarity classifier. These results suggest that, once reliable first-motion polarities are available, the accuracy of the final focal mechanism is governed primarily by the geometric constraints of the available seismic observations rather than by the CNN.

Despite the promising results presented here, several developments are still required before the proposed workflow can be integrated into a seismic monitoring routine.

The current implementation still relies on analyst-reviewed earthquake locations and manually picked P-wave arrival times. Future developments should therefore focus on integrating reliable automatic phase picking and earthquake location algorithms into the proposed workflow. Such developments would enable a fully automated processing chain, extending the computation of focal mechanisms to the large number of low-magnitude earthquakes that are currently not routinely analyzed.

Overall, this work demonstrates that a deep-learning classifier can be successfully integrated into an operational workflow for automated focal mechanism determination. This required adapting the machine-learning methodology to the constraints of the geophysical problem through region-specific training, confidence-based polarity selection, and integration with a conventional inversion algorithm. We believe that this strategy provides a practical framework for extending automated focal mechanism determination to the large number of small earthquakes that are currently beyond the reach of routine source characterization.

6 Conclusions

This study presents and validates an automated workflow for focal mechanism determination based on deep learning–derived P-wave first-motion polarities, with a specific focus on small-to-moderate earthquakes in the Italian Peninsula. By coupling a regionally trained Convolutional Neural Network (CNN) with the SKHASH algorithm, we demonstrate that machine learning can be effectively integrated into established seismological procedures to produce reliable solutions in a scalable and reproducible manner.

A key finding of this work is the critical importance of regional training data. The CNN trained on the Italian INSTANCE dataset significantly outperformed the original model trained on Californian data (CNN_CalCat). Being less conservative, the regional model successfully recovered more than 44,000 high-confidence polarities that were originally left unclassified by analysts, substantially increasing the amount of information available for focal mechanism inversion. To properly manage the proactivity of this regional model, we implemented a robust data-filtering strategy. Rather than selecting the probability threshold by maximizing a conventional machine-learning metric, we defined an operational threshold ($p \geq 0.85$) that maximizes the number of reliable polarity observations while preserving the azimuthal coverage required for robust focal mechanism solutions.

The reliability of the proposed workflow is confirmed by its agreement with the expert-reviewed TDMT catalog: 83% of the computed focal mechanisms exhibit Kagan angles smaller than 50°, with a median value of 28.7°. These results demonstrate that region-specific training significantly improves the model's ability to recognize the characteristics of Italian seismic waveforms, providing more reliable polarity estimates and, consequently, more robust focal mechanism determinations. Overall, this study provides a systematic validation of the proposed workflow across a wide range of tectonic settings in Italy.

Future work will focus on extending this workflow to near-real-time applications by integrating fully automated P-wave picking and robust earthquake location determination. By transitioning from analyst-dependent picking to fully automated, machine learning–based workflow n, this approach has the potential to substantially increase the number of reliable focal mechanism solutions routinely computed for low-magnitude earthquakes laying a foundation for next-generation, near-real-time seismic monitoring in Italy.

Data Availability

The waveforms and metadata used to train the CNN come from the INSTANCE dataset (Michelini et al., 2021, https://doi.org/10.5194/essd-13-5509-2021), accessed through the SeisBench library (Woollam et al., 2022, https://doi.org/10.1785/0220210324). The events, phase picks and manually assigned first-motion polarities forming the ItalyTest dataset were retrieved from the Italian Seismic Bulletin (BSI, https://bsi.ingv.it/); waveforms were downloaded through the INGV FDSN web services (https://terremoti.ingv.it/webservices_and_software) using ObsPy (Beyreuther et al., 2010, https://doi.org/10.1785/gssrl.81.3.530). The original CNN architecture and the Southern California training data (CalCat) are those of Ross et al. (2018, https://doi.org/10.1029/2017JB015251), available at https://scedc.caltech.edu/data/deeplearning.html. Focal mechanisms were computed with the open-source SKHASH package (Skoumal et al., 2024, https://doi.org/10.1785/0220230329; https://code.usgs.gov/esc/SKHASH), using the CIA1D velocity model (Herrmann et al., 2011), and compared with the Time Domain Moment Tensor catalog (Scognamiglio et al., 2006, https://doi.org/10.13127/TDMT; https://terremoti.ingv.it/tdmt). Event identifiers for all focal mechanism solutions shown in Figures 11 and S4 are listed in Tables S1 and S2 of the Supplementary Material.

References

1. Allen, R. (1978). Automatic earthquake recognition and timing from single traces. *Bulletin of the Seismological Society of America* 1978; 68 (5): 1521–1532. https://doi.org/10.1785/

2. Allen, R. (1982). Automatic phase pickers: Their present use and future prospects. Bulletin of the Seismological Society of America, 72(6B), S225–S242. https://doi.org/10.1785/BSSA07206B0225

3. Bernardi, F., Braunmiller, J., Kradolfer, U., & Giardini, D. (2004). Automatic regional moment tensor inversion in the European-Mediterranean region. *Geophysical Journal International*, 157, 703-716. https://doi.org/10.1111/j.1365-246x.2004.02215.x

4. Beyreuther, M., Barsch, R., Krischer, L., Megies, T., Behr, Y., & Wassermann, J. (2010). ObsPy: A Python toolbox for seismology. *Seismological Research Letters*, 81(3), 530-533. http://www.seismosoc.org/publications/SRL/SRL_81/srl_81-3_es/

5. Bishop, C. M. (2006). *Pattern Recognition and Machine Learning*. Springer New York, NY.

6. Chakraborty, M., Quinteros Cartaya, C., Li, W., Faber, J., Rümpker, G., Stoecker, H., & Srivastava, N. (2022). PolarCAP – A deep learning approach for first motion polarity classification of earthquake waveforms. *Artificial Intelligence in Geosciences*, 3, 46-52. https://doi.org/10.1016/j.aiig.2022.08.001

7. D'Amico, S., Orecchio, B., Presti, D., Gervasi, A., Zhu, L., Guerra, I., Neri, G., & Herrmann, R. B. (2011). Testing the stability of moment tensor solutions for small earthquakes in the Calabro-Peloritan Arc region (southern Italy). *Bollettino di Geofisica Teorica ed Applicata*, 52(2), 283-298. https://doi.org/10.4430/bgta0009

8. Fukushima, K. (1980). Neocognitron: A self-organizing neural network model for a mechanism of pattern recognition unaffected by shift in position. *Biological Cybernetics*, 36, 193-202. https://doi.org/10.1007/BF00344251

9. Goodfellow, I., Bengio, Y., & Courville, A. (2016). *Deep Learning*. MIT Press. https://www.deeplearningbook.org

10. Hammer, C., Beyreuther, M., & Ohrnberger, M. (2012). A seismic-event spotting system for volcano fast-response systems. Bulletin of the Seismological Society of America, 102(3), 948–960. https://doi.org/10.1785/0120110167

11. Hara, S., Fukahata, Y., & Iio, Y. (2019). P-wave first-motion polarity determination of waveform data in western Japan using deep learning. *Earth, Planets and Space*, 71. https://doi.org/10.1186/s40623-019-1111-x

12. Hardebeck, J. L., & Shearer, P. M. (2002). A new method for determining first-motion focal mechanisms. *Bulletin of the Seismological Society of America*, 92(6), 2264-2276. https://doi.org/10.1785/01200102

13. Hardebeck, J. L., & Shearer, P. M. (2003). Using S/P amplitude ratios to constrain the focal mechanisms of small earthquakes. *Bulletin of the Seismological Society of America*, 93, 2434-2444. https://doi.org/10.1785/0120020236

14. Herrmann, R. B., Malagnini, L., & Munafò, I. (2011). Regional moment tensors of the 2009 L'Aquila earthquake sequence. *Bulletin of the Seismological Society of America*, 101, 975-993. https://doi.org/10.1785/0120100184

15. ISIDe Working Group. (2007). *Italian Seismological Instrumental and Parametric Database (ISIDe)* (Version 1). Istituto Nazionale di Geofisica e Vulcanologia (INGV). https://doi.org/10.13127/ISIDE

16. Kagan, Y. Y. (1991). 3-D rotation of double-couple earthquake sources. *Geophysical Journal International*, 106(3), 709-716. https://doi.org/10.1111/j.1365-246X.1991.tb06343.x

17. Kong, Q., Trugman, D. T., Ross, Z. E., Bianco, M. J., Meade, B. J., & Gerstoft, P. (2019). Machine learning in seismology: Turning data into insights. Seismological Research Letters, 90(1), 3-14. https://doi.org/10.1785/0220180259

18. Krieger L. & Heimann S., (2012). MoPaD-Moment Tensor Plotting and Decomposition: A Tool for Graphical and Numerical Analysis of Seismic Moment Tensors, Seismological Research Letters, 83(3):589-595 https://doi.org/10.1785/gssrl.83.3.589

19. LeCun, Y., Bengio, Y., & Hinton, G. (2015). Deep learning. *Nature*, 521, 436-444. https://doi.org/10.1038/nature14539

20. Margheriti, L., Nostro, C., Cocina, O., Castellano, M., Moretti, M., Lauciani, V., Quintiliani, M., Bono, A., Mele, F. M., Pintore, S., Montalto, P., Peluso, R., Scarpato, G., Rao, S., Alparone, S., Di Prima, S., Orazi, M., Piersanti, A., Cecere, G., Cattaneo, M., Vicari, A., Sepe, V., Bignami, C., Valoroso, L., Aliotta, M., Azzarone, A., Baccheschi, P., Benincasa, A., Bernardi, F., Carluccio, I., Casarotti, E., Cassisi, C., Castello, B., Cirilli, F., D'Agostino, M., D'Ambrosio, C., Danecek, P., De Cesare, W., Della Bina, E., Di Filippo, A., Di Stefano,

R., Faenza, L., Falco, L., Fares, M., Ficeli, P., Latorre, D., Lorenzino, M. C., Mandiello, A., Marchetti, A., Mazza, S., Michelini, A., Nardi, A., Pastori, M., Pignone, M., Prestifilippo, M., Ricciolino, P., Sensale, G., Scognamiglio, L., Selvaggi, G., Torrisi, O., Zanolin, F., Amato, A., Bianco, F., Branca, S., Privitera, E., & Stramondo, S. (2021). Seismic Surveillance and Earthquake Monitoring in Italy. Seismological Research Letters, 92(3), 1659–1671. https://doi.org/10.1785/0220200380

21. Martínez-Garzón, P., Meier, M.-A., Collettini, C., Lanza, F., & Dresen, G. (2025). Stress heterogeneities governed by fault structure and stress transfer: The 2016–2017 Central Italy seismic sequence. Journal of Geophysical Research: Solid Earth, 130, e2024JB029763. https://doi.org/10.1029/2024JB029763

22. Meier, M.-A., Lanza, F., Martínez-Garzón, P., & Chiaraluce, L. (2025). Insights into extensional tectonics from a large deep learning focal mechanism catalog. Bulletin of the Seismological Society of America. https://doi.org/10.1785/0120250103

23. Meier, M. A., Ross, Z.E., Ramachandran, A., Balakrishna, A., Nair, S., Kundzicz, P., Li Z., Andrews, J., Hauksson, E., Yuel, Y. (2019) Reliable real-time seismic signal/noise discrimination with machine learning. J. Geophys. Res.: Solid Earth 124, 788–800. https://doi.org/10.1029/2018JB016661

24. Michael, A. J. Use of focal mechanisms to determine stress: a control study. J. Geophys. Res.: Solid Earth 92, 357–368 (1987). https://doi.org/10.1029/JB092iB01p00357

25. Michelini, A., Cianetti, S., Gaviano, S., Giunchi, C., Jozinović, D., & Lauciani, V. (2021). INSTANCE – the Italian seismic dataset for machine learning. *Earth System Science Data*, 13, 5509-5544. https://doi.org/10.5194/essd-13-5509-2021

26. Mousavi, S. M. & Beroza, G. C. (2020) A machine-learning approach for earthquake magnitude estimation. Geophys. Res. Lett. 47. https://doi.org/10.1029/2019GL085976

27. Mousavi, S. M., Ellsworth, W. L., Zhu, W., Chuang, L. Y., Beroza, G. C. (2020). Earthquake transformer—an attentive deep-learning model for simultaneous earthquake detection and phase picking. Nature Communications 11, 1–12.https://doi.org/10.1038/s41467-020-17591-w

28. Mousavi, S. M., Horton, S. P., Langston, C. A., & Samei, B. (2016). Seismic features and automatic discrimination of deep and shallow induced-microearthquakes using neural network and logistic regression. *Geophysical Journal International*, 207(1), 29–46. https://doi.org/10.1093/gji/ggw258

29. Nanjo, K. Z. (2020) Were changes in stress state responsible for the 2019 Ridgecrest, California, earthquakes? Nat. Commun. 11, https://doi.org/10.1038/s41467-020-16867-5

30. Perol, T., Gharbi, M., Denolle, M. (2018). Convolutional neural network for earthquake detection and location. Science Advances, 4(2):e1700578. https://doi.org/10.1126/sciadv.170057

31. Pondrelli, S., Salimbeni, S., Ekström, G., Morelli, A., Gasperini, P., & Vannucci, G. (2006). The Italian CMT dataset from 1977 to the present. *Physics of the Earth and Planetary Interiors*, 159, 286-303. https://doi.org/10.1016/j.pepi.2006.07.008

32. Powers, D. M. W. (2011). Evaluation: From Precision, Recall and F-measure to ROC, Informedness, Markedness and Correlation. Journal of Machine Learning Technologies, 2(1), 37-63.

33. Ross, Z. E., Meier, M.-A., & Hauksson, E. (2018). P-wave arrival picking and first-motion polarity determination with deep learning. *Journal of Geophysical Research: Solid Earth*, 123. https://doi.org/10.1029/2017JB015251

34. Satriano, C., Wu, Y.-M., Zollo, A., & Kanamori, H. (2011). Earthquake early warning: Concepts, methods and physical grounds. *Soil Dynamics and Earthquake Engineering*, 31(2), 106–118. https://doi.org/10.1016/j.soildyn.2010.07.007

35. Scognamiglio L., Tinti E., & Michelini A. (2009). Real-time determination of seismic moment tensor for the Italian region. *Bulletin of the Seismological Society of America*, 99(4), 2223-2242. https://doi.org/10.1785/0120080104

36. Scognamiglio L., Tinti E., & Quintiliani M. (2006). *Time Domain Moment Tensor (TDMT)* [Data set]. Istituto Nazionale di Geofisica e Vulcanologia (INGV). https://doi.org/10.13127/TDMT

37. Skoumal, R. J., Hardebeck, J. L., & Shearer, P. M. (2024). SKHASH: A Python package for computing earthquake focal mechanisms. *Seismological Research Letter*, 95(4), 2519-2526. https://doi.org/10.1785/0220230329

38. Steinberg, A., Vasyura-Bathke, H., Gaebler, P., Ohrnberger, M., & Ceranna, L. (2021). Estimation of seismic moment tensors using variational inference machine learning. *Journal of Geophysical Research: Solid Earth*, 126, e2021JB022685. https://doi.org/10.1029/2021JB022685

39. Uchide, T. (2020). Focal mechanisms of small earthquakes beneath the Japanese islands based on first-motion polarities picked using deep learning. *Geophysical Journal International*, 223, 1658-1671. https://doi.org/10.1093/gji/ggaa401

40. Wang, X. & Zhan, Z. Seismotectonics and fault geometries of the 2019 ridgecrest sequence: insight from aftershock moment tensor catalog using 3-D Green's functions.(2020) J. Geophys. Res.: Solid Earth 125, https://doi.org/10.1029/2020JB019577

41. Woollam, J., Münchmeyer, J., Tilmann, F., Rietbrock, A., Lange, D., Bornstein, T., Diehl, T., Giunchi, C., Haslinger, F., Jozinović, D., Michelini, A., Saul, J., & Soto, H. (2022). SeisBench - A toolbox for machine learning in seismology. *Seismological Research Letters*. https://doi.org/10.1785/0220210324

42. Zhao, M., Xiao, Z., Zhang, M., Yang, Y., Tang, L., & Chen, S. (2023). DiTingMotion: A deep-learning first-motion-polarity classifier and its application to focal mechanism inversion. *Frontiers in Earth Science*, 11, 335. https://doi.org/10.3389/feart.2023.1103914

43. Zhu W., Beroza G.C., PhaseNet: a deep-neural-network-based seismic arrival-time picking method, *Geophysical Journal International*, Volume 216, Issue 1, January 2019, Pages 261–273, https://doi.org/10.1093/gji/ggy423

Supplementary Material

S1. CNN Training History

Fig. S1 depicts the training progression of the CNN_INSTANCE model, showing the evolution of loss and accuracy over epochs. The curves demonstrate a stable convergence, characterized by a steep initial improvement followed by a plateau, indicating effective feature learning. Crucially, the validation metrics (red lines) closely track the training metrics (black lines); this alignment suggests that the model generalizes well to unseen data without suffering from significant overfitting. This stability confirms the effectiveness of the applied data augmentation and balancing strategies.

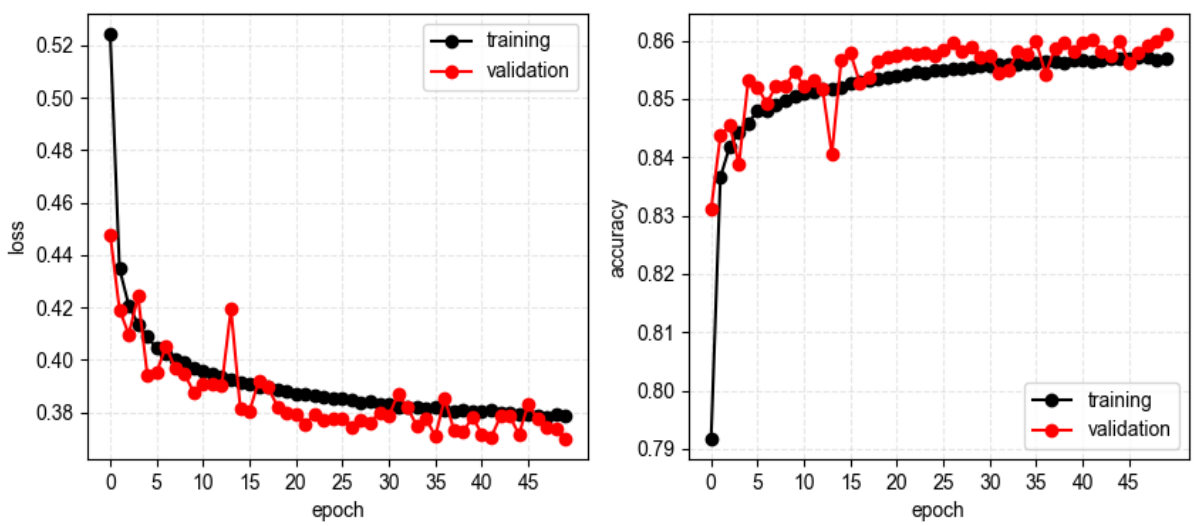

Figure S1. Training history for the CNN_INSTANCE model.

S2. CNN_Instance and CNN_CalCat comparison

S2.1 Confusion Matrix for CNN_CalCat

We compared the performance of CNN_INSTANCE with CNN_CalCat to evaluate the impact of using two distinct training datasets on the final classification accuracy. The comparison is performed by testing the predictive capability of CNN_CalCat on the ItalyTest dataset. The evaluation relies on standard metrics and confusion matrices to provide a detailed breakdown of the error distribution and to verify the consistency of the predictions against the ground truth catalog. In Fig. S2, we show the confusion matrix related to CNN_CalCat model.

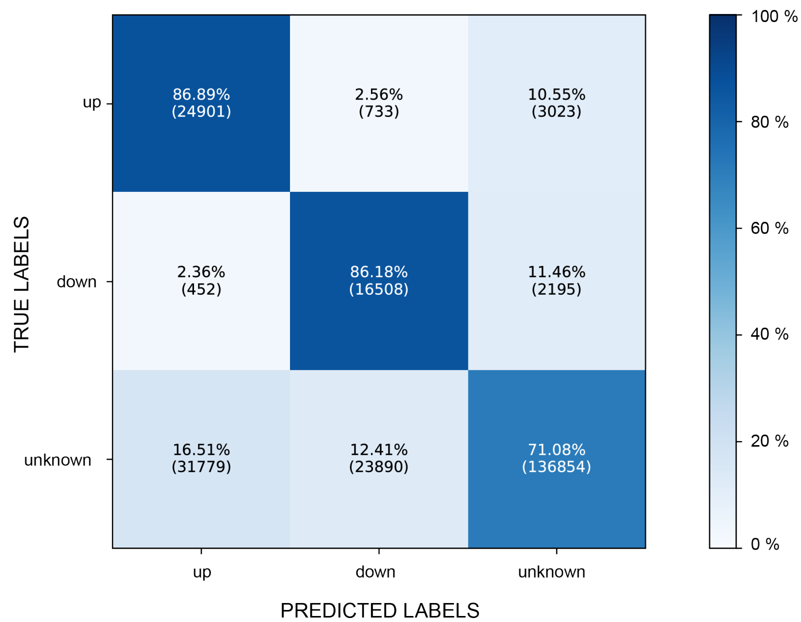

Figure S2. Confusion matrix obtained by testing the CNN_CalCat model on the ItalyTest dataset. Each class shows the percentage of the total number of predictions, with the corresponding number of traces reported in brackets (each row sums to 100%).

The comparison between the two models reveals distinct predictive behaviors. The CNN_CalCat shows a comparable overall accuracy (97%) and precision, primarily due to a more conservative classification strategy. However, this comes at the expense of a lower recall (86.8% for “up” polarities), as the model frequently assigns an ”unknown” label to waveforms with identifiable polarities.

In contrast, CNN_INSTANCE, observing the confusion matrix in Fig.3 of the main text, demonstrates a superior balance between precision and recall. While maintaining high classification precision (95.6% for “up” and 93% for “down”), it achieves a significantly higher recall (91.5% and 90%, respectively). This indicates that CNN-INSTANCE is more effective at recovering polarity information from the Italian dataset, providing a larger and more complete set of first-motion observations. For the purpose of focal mechanism inversion, where maximizing the number of reliable polarities is crucial, CNN-INSTANCE proves to be the more performant and suitable model.

S2.2 Probability threshold for CNN_CalCat

To achieve a consistent comparison between the two models, we evaluated the performance of the CNN_CalCat model under the same data-retention criterion. Specifically, to retain approximately 80% of the polarity estimates, while achieving high precision values (higher than 98%), a probability threshold of 0.6 is required for the CNN_CalCat model. This lower threshold, compared to the one adopted for the INSTANCE-trained model, implies a reduced confidence level in the retained predictions. Fig. S3 shows the resulting confusion matrix.

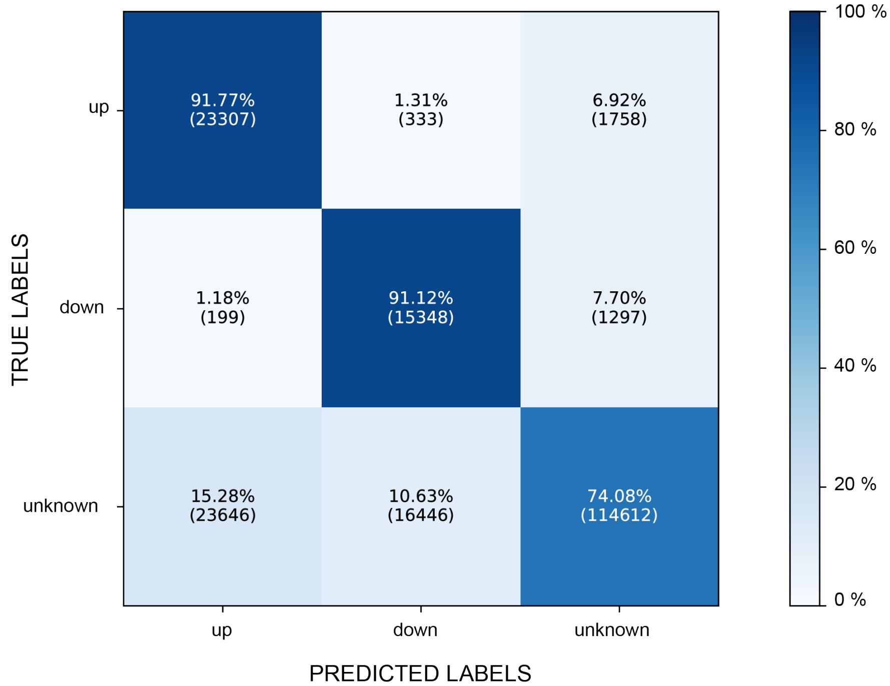

Figure S3. Confusion matrix obtained by testing the CNN_CalCat model on the ItalyTest dataset, considering only classifications with a probability higher than 60%. Each class shows the percentage of the total number of predictions, with the corresponding number of traces given in brackets (each row sums to 100%).

While the CNN_CalCat model exhibits very high precision, at the best-observed value of 99.15% for the class “up”, this strict filtering leads to a serious loss in data, which consequently drops recall to 91.7% and 91% for “up” and “down” polarities, respectively. On the other hand, the CNN_INSTANCE model, tuned on an optimal confidence probability threshold of 0.85 to retain ~80% of the data, manages to preserve a precision comparable with that of CNN_CalCat at 98.4% for “up” and 97.9% for “down” while giving notably higher recall values of 97.9% and 96.8%. This increase in performance is due to the network's capability to resolve ambiguity. It indeed recovers a significant fraction of waveforms classified as “unknown” by CNN_CalCat and assigns them a definitive polarity with high confidence. The marginal reduction of precision in the “up” class is then balanced by the volume of additional valid data. In this way, the +7.5% of data recovery represents an advantageous trade-off because it is crucial for minimizing azimuthal gaps and constraining the focal solutions for a wider range of seismic events.

Moreover, when the probability threshold value of 0.85 is used on the CNN_CalCat model, we end up retaining just 62.2% of our data. Although for these data we obtain corresponding precision and recall values comparable to CNN_INSTANCE (i.e. 99% precision for both classes "up" and "down"; 97.8% and 98.2% recall for "up" and "down" classes, respectively), success is achieved on just a subset of our data. The drastic reduction in retained data suggests that there might be a high chance of discarding classifications that would be important in the calculation of the focal mechanisms.

S3. Focal mechanism analysis

While 65% of our focal mechanisms show strong agreement with the TDMT catalog (71% if we include the acceptable Kagan angle range 40°-45), 88 events exhibit larger discrepancies, with Kagan angles exceeding 40° (Fig. S4). These differences do not necessarily imply that the CNN-derived polarities are incorrect, but rather highlight the inherent methodological and observational challenges in source characterization. Based on our analysis and recent literature (e.g., Cheng et al., 2023; Zhao et al., 2023), we attribute part of these discrepancies to three main factors:

1. The projection of the polarities onto the focal sphere. Specifically, while the azimuth determines the angular distribution around the epicenter, the takeoff angle reflects the range of epicentral distances of the recording stations relative to the source. To evaluate the effect of the vertical distribution of the stations, we introduced a variable called "takeoff spread". This parameter represents the difference between the takeoff angles of the farthest and the closest stations used

in the polarity dataset. As shown in Fig. S6 (Fig. S5, Panel A), events with Kagan angles exceeding 40° consistently exhibit a reduced takeoff spread. This indicates that the stations contributing to the focal mechanism inversion are clustered within a limited range of epicentral distances. Geometrically, this results in the concentration of polarities within a narrow ring on the focal sphere, a configuration that fails to adequately constrain the nodal planes and leads to increased solution instability.

2. Number of available polarities. Events characterized by a Kagan angle greater than 40° typically show a lower number of predicted polarities. There is a trend in which a reduced number of observations corresponds to a decrease in the overall fit of the focal mechanism (Fig. S5, Panel B).

3. Polarity imbalance. Another source of inaccuracy in focal mechanism solutions is the presence of significant polarity imbalance. We define this condition as a situation in which a dominant portion of the predicted polarities belongs to a single class (“up” or “down”), with only a small fraction representing the opposite case. This lack of polarity diversity does not provide sufficient constraints on the nodal planes and often leads to high Kagan angles (>40°). To quantify this effect, we analyzed the probability density distribution of polarity imbalance, focusing on the range from 70% (moderate imbalance) to 100% (total imbalance) (Fig. S5, Panel C). The green curve, corresponding to Kagan angles ≤40°, shows a clear peak around 75% imbalance, after which the probability decreases steadily. The red curve, corresponding to Kagan angles >40°, is broader

and shifted toward higher imbalance values, indicating that unstable solutions become much more frequent when polarity imbalance exceeds 85%.

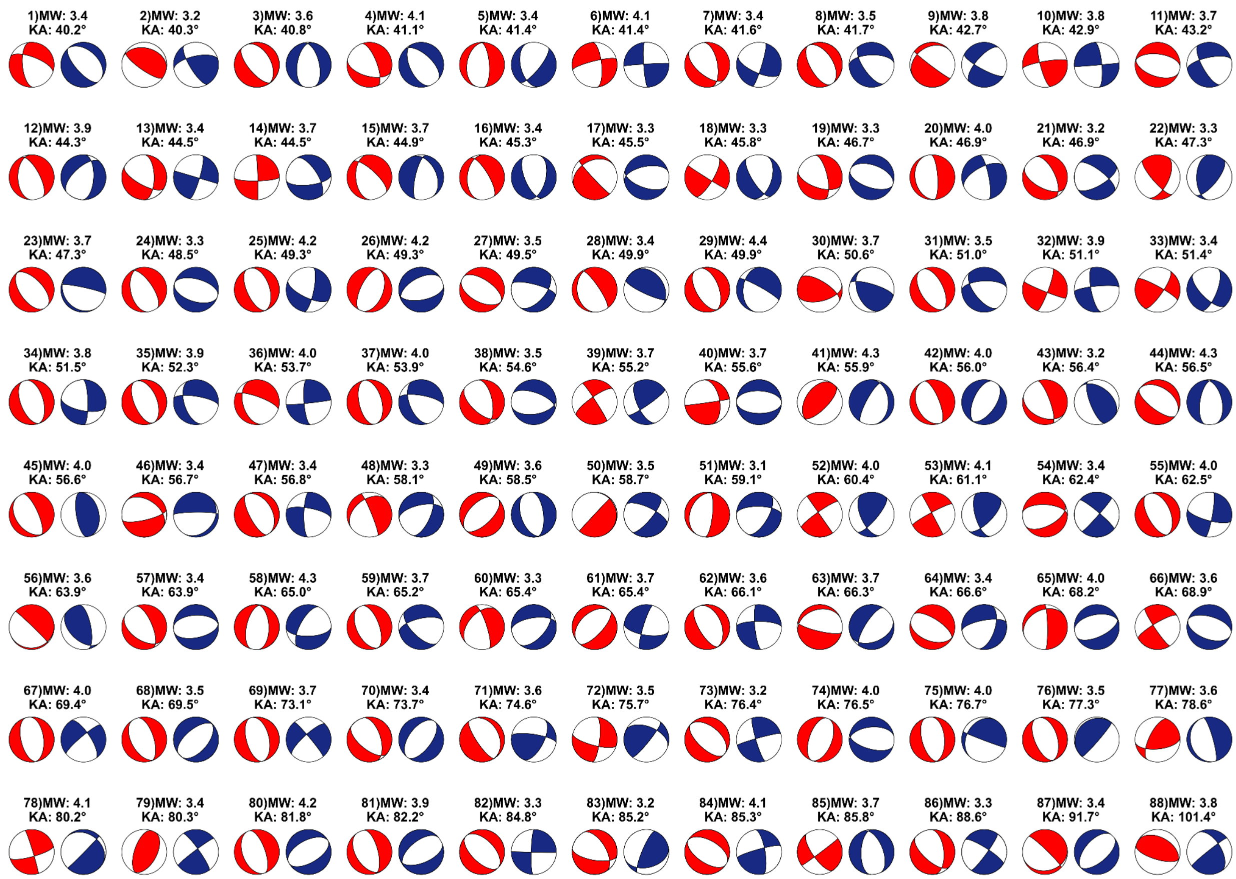

Figure S4. Comparison of 88 events with Kagan angles greater than 40° between the predicted and TDMT focal mechanism solutions. Solutions computed with the proposed methodology are shown in blue, while those from the TDMT catalog are shown in red. For each pair, the moment magnitude (Mw) and the corresponding Kagan angle (K.A.) are reported above.

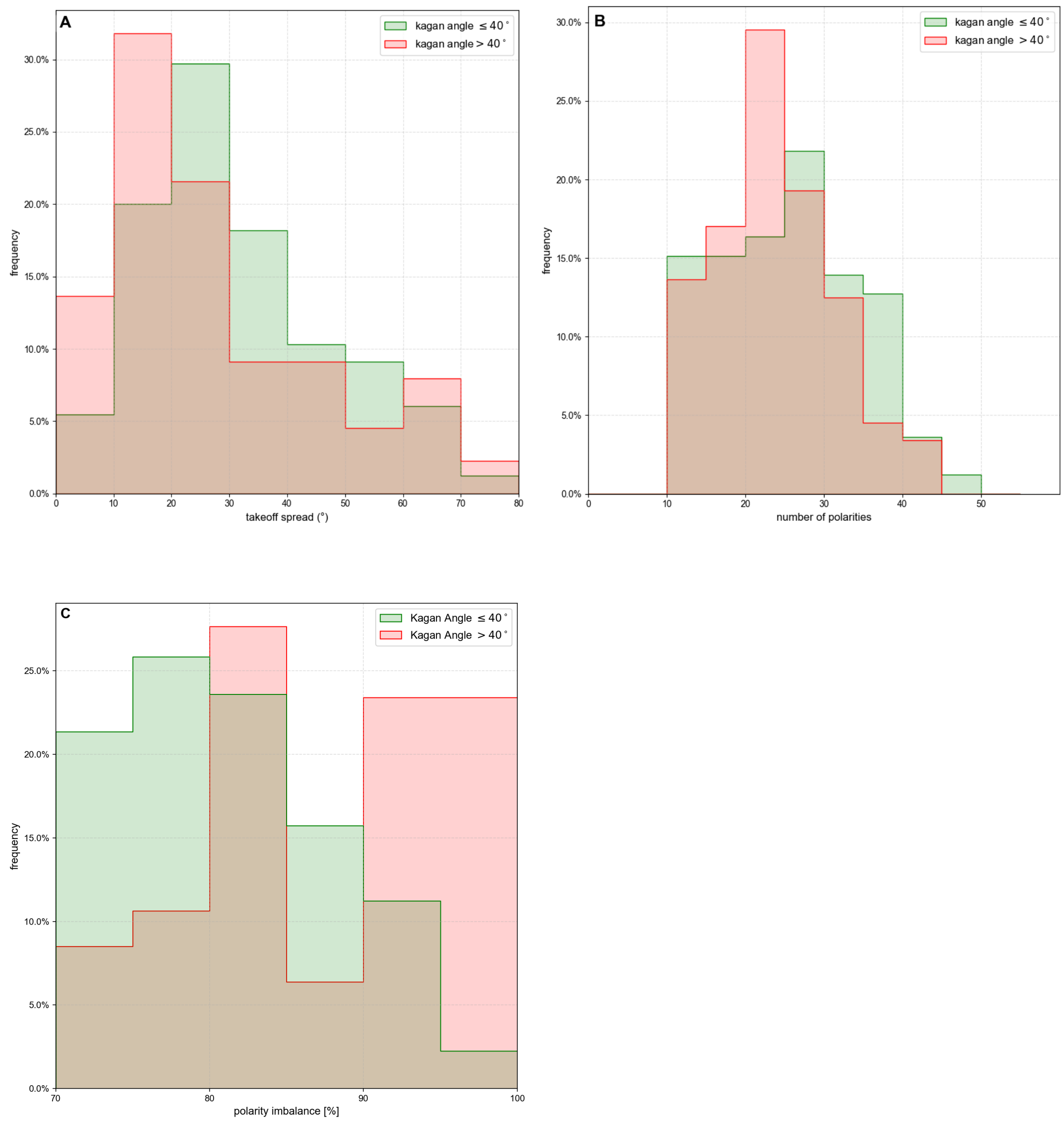

Figure S5. Panel A: Distribution of the angular coverage of the focal sphere for events with Kagan angles lower than 40° (green) and greater than 40° (red). The red distribution is more peaked around 10°–20°, whereas events with lower Kagan angles show a broader distribution of takeoff spread. Panel B: Frequency distribution of the number of used polarities for events with Kagan angles less than or equal to 40° (green) and greater than 40° (red). Panel C: Distribution of events as a function of polarity imbalance.

number	event_id	number	event_id	number	event_id	number	event_id	number	event_id
1	8904671	34	18998161	67	38471201	100	20652011	133	7154631
2	7490751	35	29226401	68	4002881	101	21324301	134	7082751
3	8881771	36	7079501	69	6376371	102	2919691	135	8315871
4	22984881	37	15404071	70	13107321	103	8315581	136	8363661
5	7082291	38	36163521	71	34293041	104	38928171	137	18608661
6	7261821	39	21373071	72	5884121	105	7241751	138	23414191
7	7112411	40	19395691	73	7083361	106	30543871	139	7182461
8	23137151	41	38844781	74	23551301	107	16117541	140	18596591
9	20328561	42	17543261	75	28008151	108	32988201	141	3429721
10	10763951	43	7478701	76	28455251	109	7284031	142	18768031
11	13552951	44	10856611	77	30682211	110	9759131	143	7475861
12	4975321	45	21474351	78	17769831	111	12826461	144	19580441
13	29810561	46	7097951	79	7159911	112	25829601	145	14288901
14	30904161	47	38252891	80	35754081	113	19422381	146	4044341
15	5271921	48	10674861	81	24128501	114	25344471	147	34089381
16	23558121	49	40796701	82	3668911	115	37547911	148	22855201
17	8879831	50	6431031	83	7089821	116	24517581	149	15656321
18	9472991	51	15529391	84	29284471	117	3684841	150	16916801
19	26679671	52	3716391	85	12723601	118	12837731	151	34161341
20	22524231	53	7078371	86	5812451	119	34297281	152	7021651
21	20110741	54	4495131	87	8587901	120	6381251	153	5717681
22	2984451	55	8706291	88	34702701	121	13708811	154	6861601
23	8130121	56	19004961	89	28650151	122	22864191	155	14721181
24	7105011	57	6258121	90	32824731	123	20379371	156	27189251
25	3919881	58	8728691	91	25025251	124	12269701	157	23606591
26	31033941	59	37989201	92	12712641	125	14721631	158	38576831
27	15789461	60	27575091	93	14933511	126	8694191	159	14950321
28	23551771	61	9151161	94	16959571	127	32830781	160	3097811
29	8128111	62	18562301	95	18224991	128	18717581	161	18389661
30	37564121	63	24272751	96	17474201	129	35473031	162	23605481
31	7083031	64	8954461	97	36868511	130	8887571	163	6476631
32	8692821	65	24397691	98	8676191	131	7339051	164	14725141
33	34297011	66	4326711	99	25142861	132	7131591	165	28436891

Table S1. Table mapping the list of 165 event numbers and the corresponding event_id on the https://terremoti.ingv.it/ website.

number	event_id	number	event_id	number	event_id	number	event_id
1	12736301	23	17025201	45	3678251	67	15023141
2	7225951	24	7326791	46	24844501	68	7343051
3	6880121	25	13276121	47	18019191	69	18360641
4	5025051	26	7343701	48	7085981	70	7363391
5	16031391	27	22882061	49	22338321	71	16145051
6	32478631	28	13043881	50	32594971	72	30997491
7	13086621	29	7081331	51	9195441	73	8344901
8	13314821	30	20443471	52	33982091	74	23231121
9	10027911	31	8419711	53	33991441	75	15023211
10	25881981	32	14932631	54	37545981	76	13321561
11	13436511	33	16975931	55	13274891	77	4130781
12	7077321	34	13280161	56	12716291	78	4694251
13	7202351	35	8427061	57	8185181	79	5698891
14	30900271	36	16415301	58	23997291	80	7122651
15	12706731	37	8538851	59	7345471	81	7474911
16	14672421	38	18678961	60	7226481	82	7789041
17	17400021	39	33993041	61	25750091	83	18525891
18	16838451	40	19103491	62	7213761	84	6765511
19	7405941	41	33063421	63	4117291	85	6984921
20	8949131	42	7141891	64	22883481	86	3890121
21	7274021	43	7090771	65	8936321	87	20404571
22	25149791	44	4875411	66	18726131	88	37643051

Table S2. Table mapping the list of 88 event numbers with Kagan angle higher than 40° and their corresponding event_id on the https://terremoti.ingv.it/ website.